5089

ANNUAL REPORT

Contract MO-AO1-78-00-4335
NOAA/NESS/SPOC Group
United States Department of Commerce
January 1982

THE BERING SEA ICE COVER DURING MARCH 1979: COMPARISON OF SURFACE AND SATELLITE DATA WITH THE NIMBUS-7 SMMR

Seelye Martin
School of Oceanography WB-10
University of Washington
Seattle, Washington 98195

Donald J. Cavalieri
Per Gloersen
Goddard Laboratory for Atmospheric Sciences
NASA/Goddard Space Flight Center
Greenbelt, Maryland 20771

S. Lyn McNutt
School of Oceanography WB-10
University of Washington
Seattle,Washington 98195

School of Oceanography
University of Washington
Seattle, WA 98195

Ref: A82-4

TABLE OF CONTENTS

1. Introduction 1

2. Support Observations 1

2.1 Data Sources 2

2.2 The Weather 4

2.3 The Nature of the Ice Edge 6

2.4 The Tires Ice Charts 10

3. The SMMR Imagery 13

3.1 SMMR Radiances 13

3.2 Ice Algorithm 16

3.3 Spatial Resolution of Data 19

4. Comparison of Data 20

4.1 3 March (day 62) 20

4.2 9 March (day 68) 28

4.3 15 March (day 74,75) 33

4.4 25 March (day 74) 39

5. Concluding Remarks 42

6. Acknowledgments 44

7. Bibliography 46

Appendix A 47

Appendix B 49

1. INTRODUCTION

During March 1979, field operations were carried out in the Marginal Ice Zone (MIZ) of the Bering Sea. The field measurements which included oceanographic, meteorological, and sea ice. observations were made nearly coincident with a number of Nimbus-7 and Tires-N satellite observations .

This report presents the results of a comparison between surface and aircraft observations, and images from the Tires-N satellite, with ice concentrations derived from the microwave radiances of the Nimbus-7 Scanning Multichannel Microwave Radiometer (SMMR). Following a brief discussion of the field operations, including a summary of the meteorological conditions during the experiment, we describe the satellite data with emphasis on the Nimbus-7 SMMR and the physical basis of the algorithm used to retrieve ice concentrations; We then carry out a detailed comparison for four days in March of the SMMR imagery with all available surface, satellite, and meteorological data. The results of this study show that the SMMR-derived ice concentrations provide nearly all-weather information on both the ice edge position and the location of low and high ice concentrations within the Bering Sea pack ice.

2. SUPPORT OBSERVATIONS

The present section describes the surface, aircraft, weather, and satellite data used for comparison with the results of the SMMR algorithm. Specifically, 52.1 summarizes the data sources and §2.2 gives an overview of the weather and the general ice behavior. Then, because the Bering Sea ice edge is not an abrupt transition from open ocean to solid ice, but rather a gradual transition which affects the SMMR ice

edge resolution, §2.3 gives a physical description of the ice edge. Next, §2.4 describes the Tires images, and the way in which we prepared the ice charts from these images. Finally, throughout the report, we give all dates in terms of Julian days and Greenwich Mean Time, so that 2 March, 1200 G.M.T., for example, is Julian day 62:1200.

2.1 Data Sources

As part of the Bureau of Land Management/National Oceanic and Atmospheric Administration (NOAA) Outer Continental Shelf Program, the NOAA ship SURVEYOR carried out a survey of the properties of the Bering Sea Marginal Ice Zone (MIZ) in the region between Nunivak and St. Matthew Islands from 1 - 14 March 1979 (Figure 1). Several papers and reports describe the results of this cruise. Pease (1979) gives an overview of meteorology and oceanography of the Bering Sea, with partitular reference to the region surveyed by the cruise.

Second, Salo et al. (1980) list all of the-oceanographic and meteorological data taken during the cruise, and give maps of both surface level pressure and air temperature, and surface level pressure and winds at 12 hour intervals for 1 - 31 March. Third, Squire & Moore (1979) give the results of their ocean swell attenuation by pack ice experiment. Fourth, Bauer & Martin (1980) give a complete description of the ice edge properties at distances of up to 50 km into the pack, and also describe the formation and movement of the ice edge bands. Fifth, Martin & Kauffman (1979) give descriptions of all ice cores taken during the cruise plus core photographs and surface and aerial site photographs. Finally, from a related study, McNutt (1980) gives a detailed ice description based on satellite and aircraft observations.

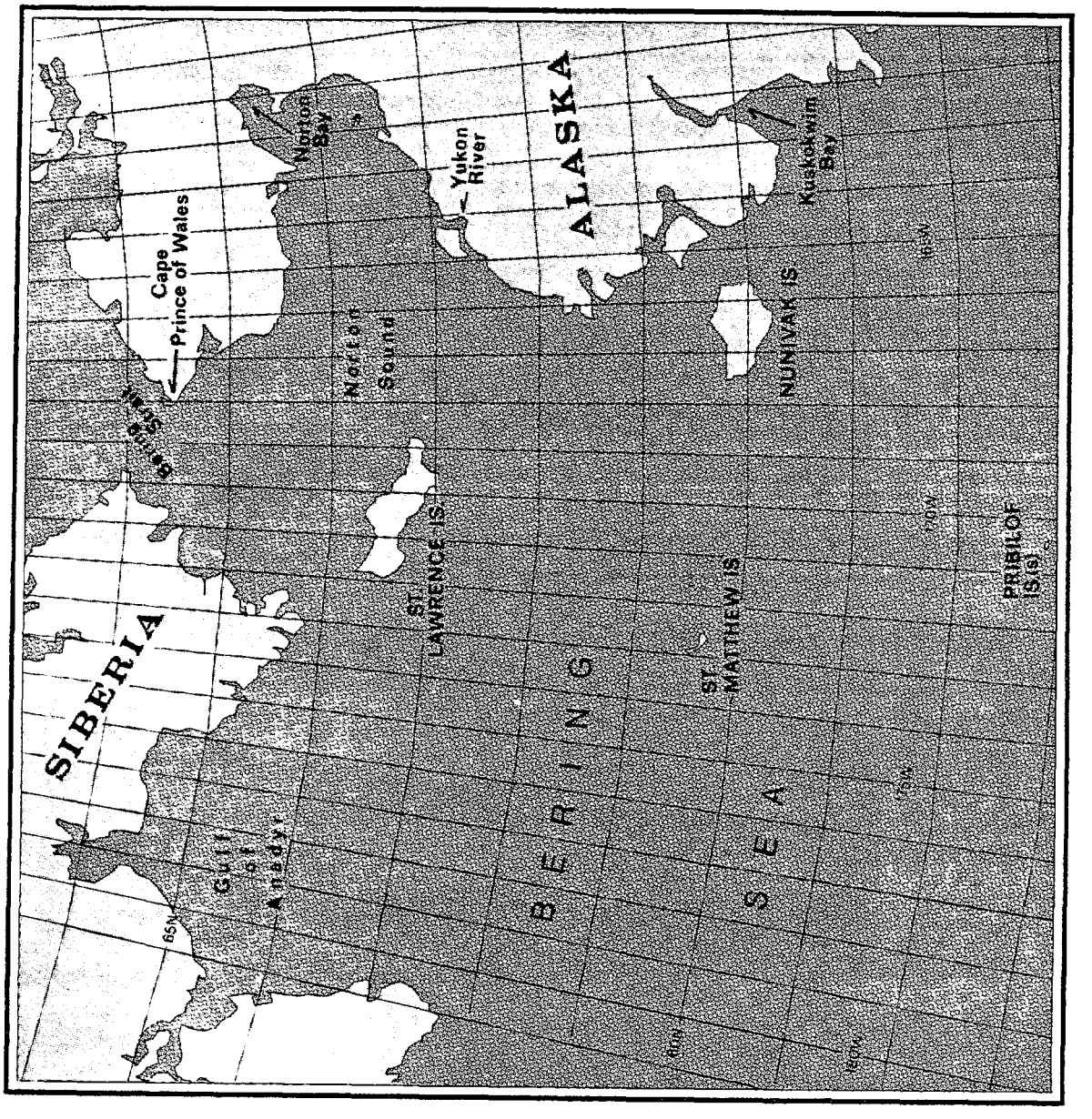

Figure 1. Base Map.

The data used to verify the SMMR output then, consists of the following:

1. Surface observations of ice thickness and concentration carried out by helicopter from the NOAA ship SURVEYOR are described in Bauer & Martin (1980) and Martin & Kauffman (1979).

2. P-3 ice reconnaissance overflights on 3 and 9 March give ice edge position and the location of some interior features from visual and classified radar observations. Appendices A and B give the verbatum ice reconnaissance messages.

3. Surface level pressure and winds are from Appendix C of Salo et al. (1980). This data is re-analyzed from maps produced by the National Weather Service Field Office in Anchorage, Alaska.

4. Tires Imagery was made available by the the NOAA Environmental Satellite Services Field Office in Anchorage.

5. Ice Charts are prepared from the Tires images by the method described in 52.4.

2.2 The Weather

We take our weather analysis from the maps and discussion of Salo et al (1980). Following their Appendix 3, the weather in the southern Bering Sea divides into two parts during March 1979. First, from 1 - 19 March (60:0000 - 78:1200), the Siberian high pressure system dominated the Bering Sea. During this period, the winds were cold and from the north to northeast direction, with only a few 12 hour interruptions caused by lows moving along the Aleutians (Figures 2a - 2c). Beginning 20 March (79:0000) through the end of the month, a large low pressure system centered over the western Aleutians caused warm southerly winds to flow up into the Bering (Figure 2d). The predominant winds in the eastern Bering Sea were then from the southwest, and the ice retreated.

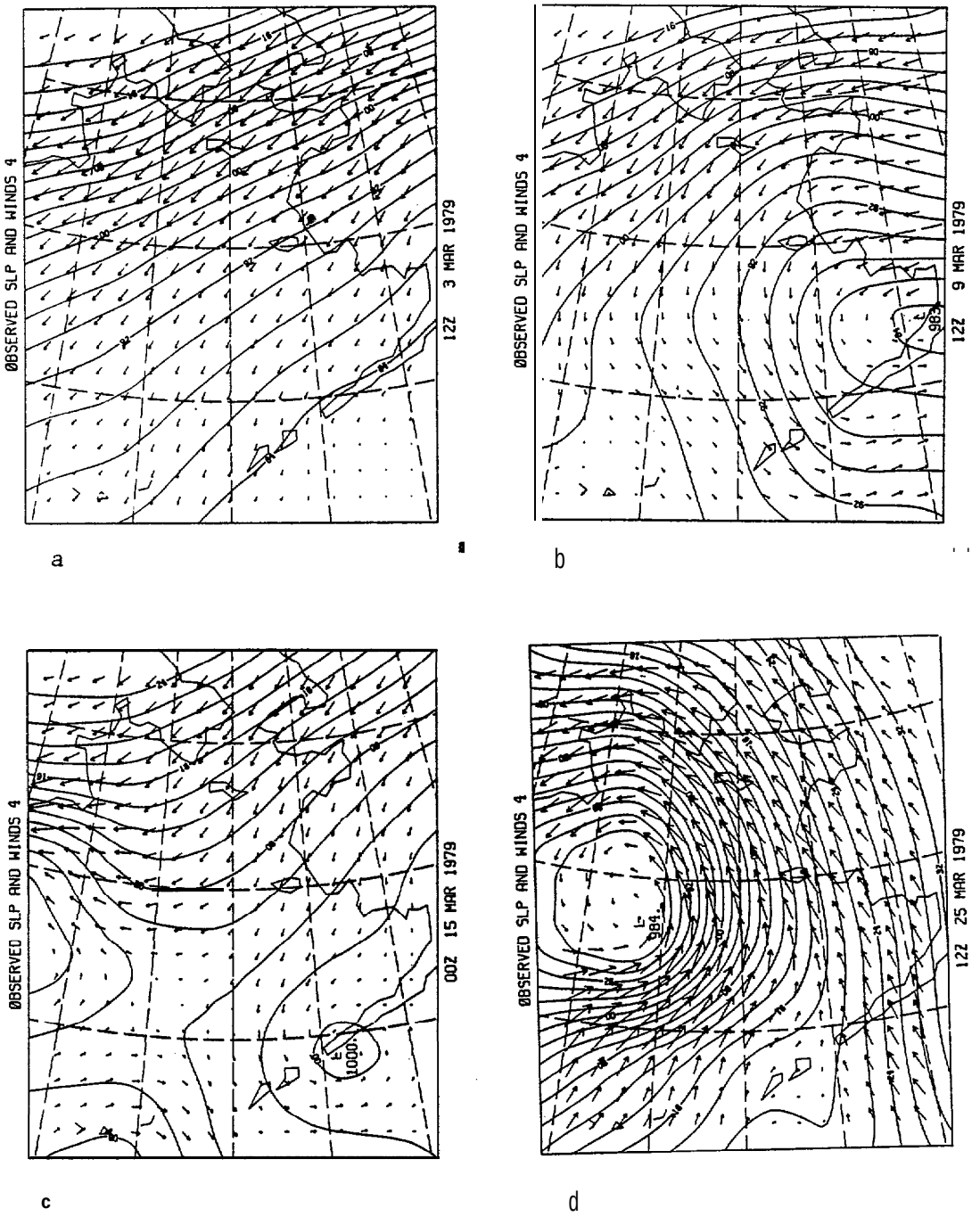

Figure 2. Observed surface level pressure and winds for March 1979 (from Salo et al. 1980). The longest wind vector is 20 m S-l. (a) 62:1200; (b) 68:1200; (c) 74:0000; (d) 84:1200.

Because of partially clear weather during 1 - 19 March, Tires satellite imagery of the ice was available, although the oblique satellite orbit caused bad distortion on some images. From 20 - 25 March, the Bering Sea was completely cloud -covered, with the first clear image on 25 March (day 84) showing a dramatic ice retreat. During this first period of north to northeast winds, the ice which moved to the right of the wind, in general advanced southwest away from the Alaska mainland and the islands. During the southerly wind period the ice retreated dramatically up into Norton Sound.

2.3 The Nature of the Ice Edge

During the cruise period, Bauer & Martin (1980) describe the ice edge appearance as observed along three section lines. Figure 3 gives an idealized picture of the ice edge. Because of both the propagation of ocean swell into the pack, and its attenuation by the pack ice, Squire & Moore (1979) show that the MIZ divides Into three distinct zones called respectively the 'edge' , 'transition', and 'interior' zones.

In the edge zone, the ocean swell fractures the floes and causes them to raft and ridge into irregularly shaped floes with diameters of about 20 m and thicknesses of 1-4 m (Figure 4). In the transition zone the swell fractures the floes, but does not raft and ridge them, so that the ice has a regular rectangular pattern with the long axis of the rectangle at right angles to the swell propagation direction (Figure 5). In the interior zone, the swell amplitude is sufficiently reduced such that it propagates through the floes without fracturing them, so that the floes have widths of order km, and thicknesses of 0.2 - 0.3 m (Figure 6). We observed some form of this idealized ice distribution on

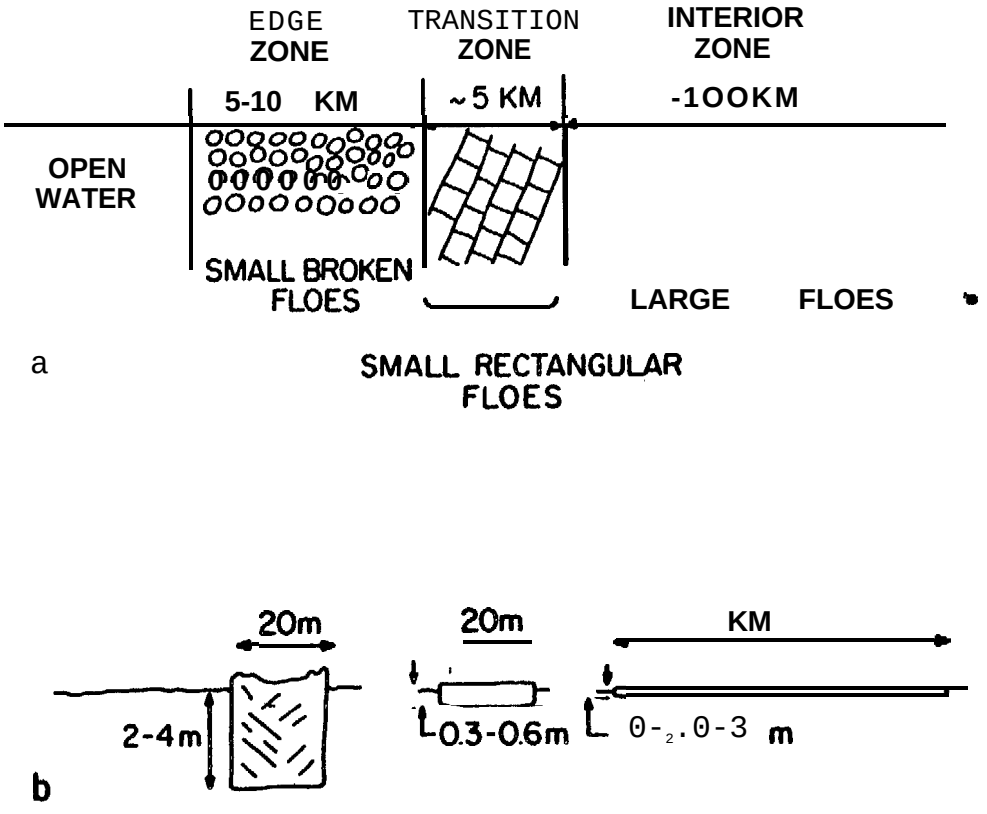

Figure 3. A schematic diagram of the three kinds of ice which occur near the ice edge, proceeding inward from open water. The upper part of the figure shows the ice in plan view; the lower part, in side view ([from Bauer & Martin (1980, Figure 2)].

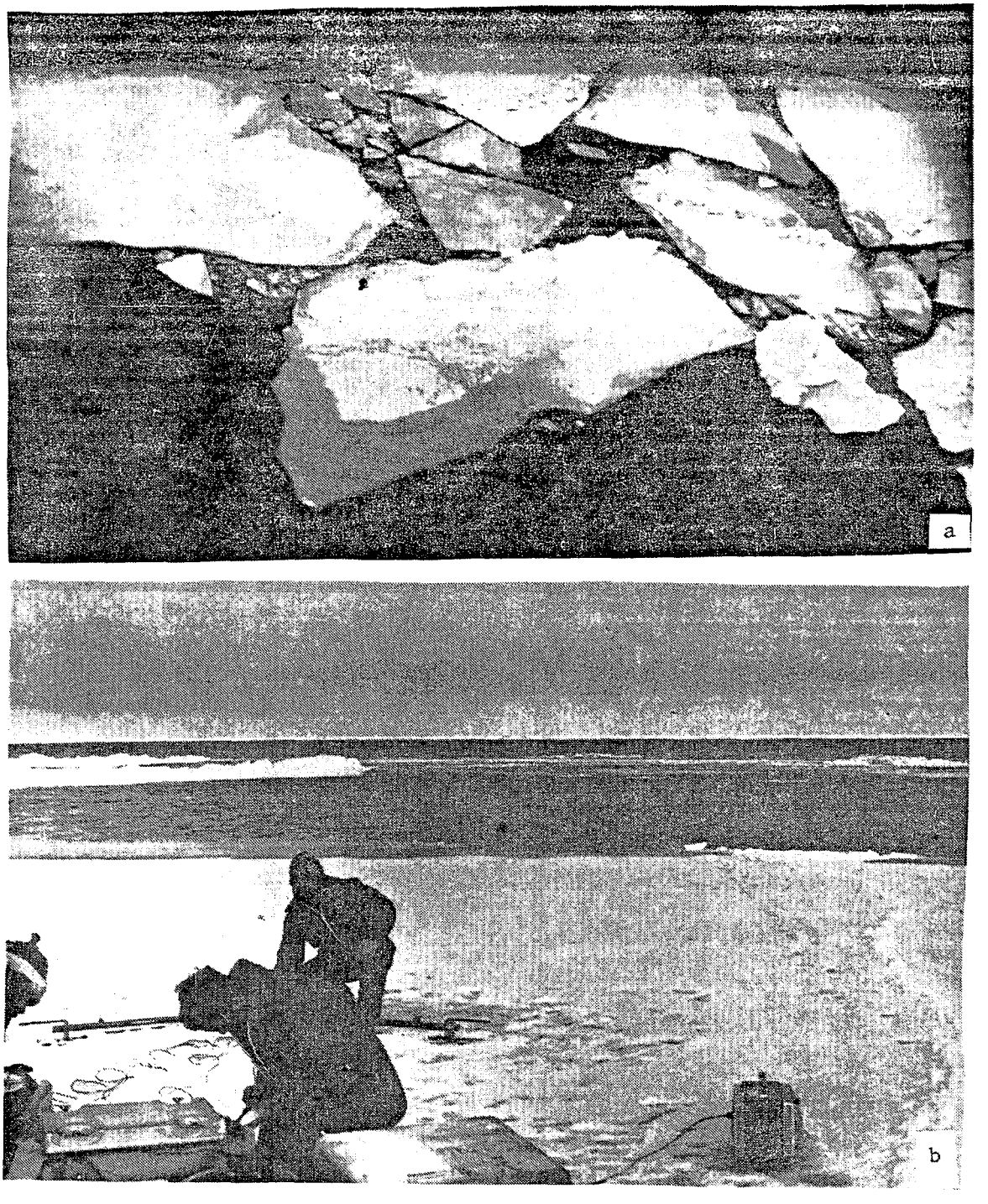

Figure 4. Floes in the edge zone on 6 March 1979 (day 65). (a) Aerial view from 60 m; large floe in foreground measures 20 by 40 m^2; (b) surface view of large floe looking toward dark area in foreground of (a); seal is in water. From divers' observations, this floe is 1-5 m thick [from Bauer & Martin (1980) and Martin & Kauffman (1979)].

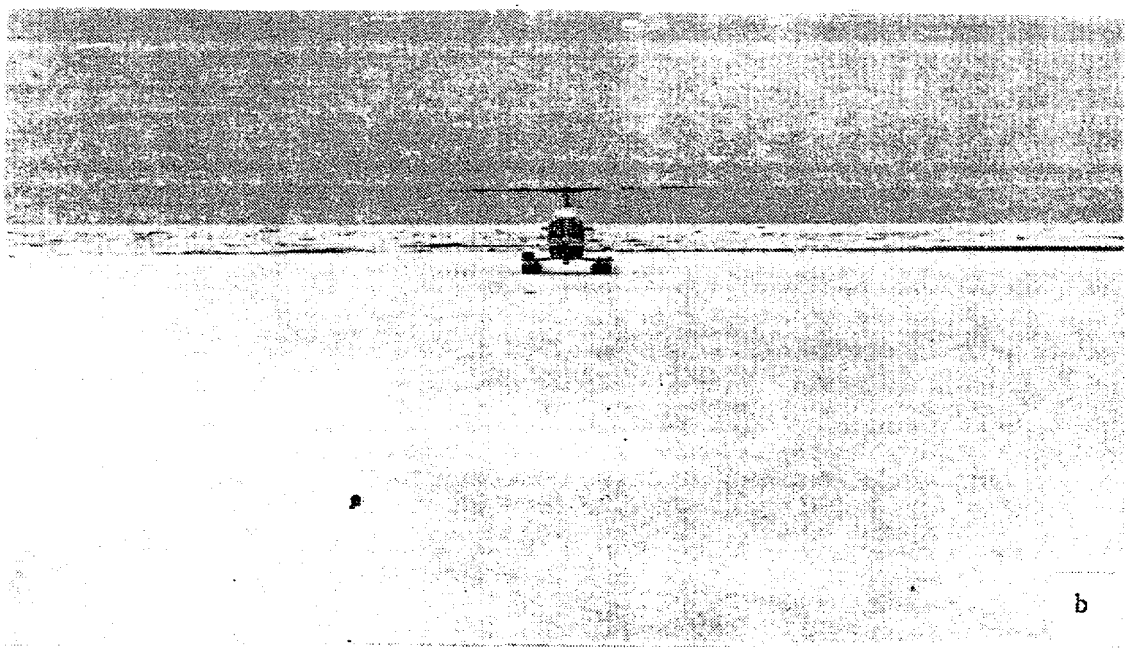

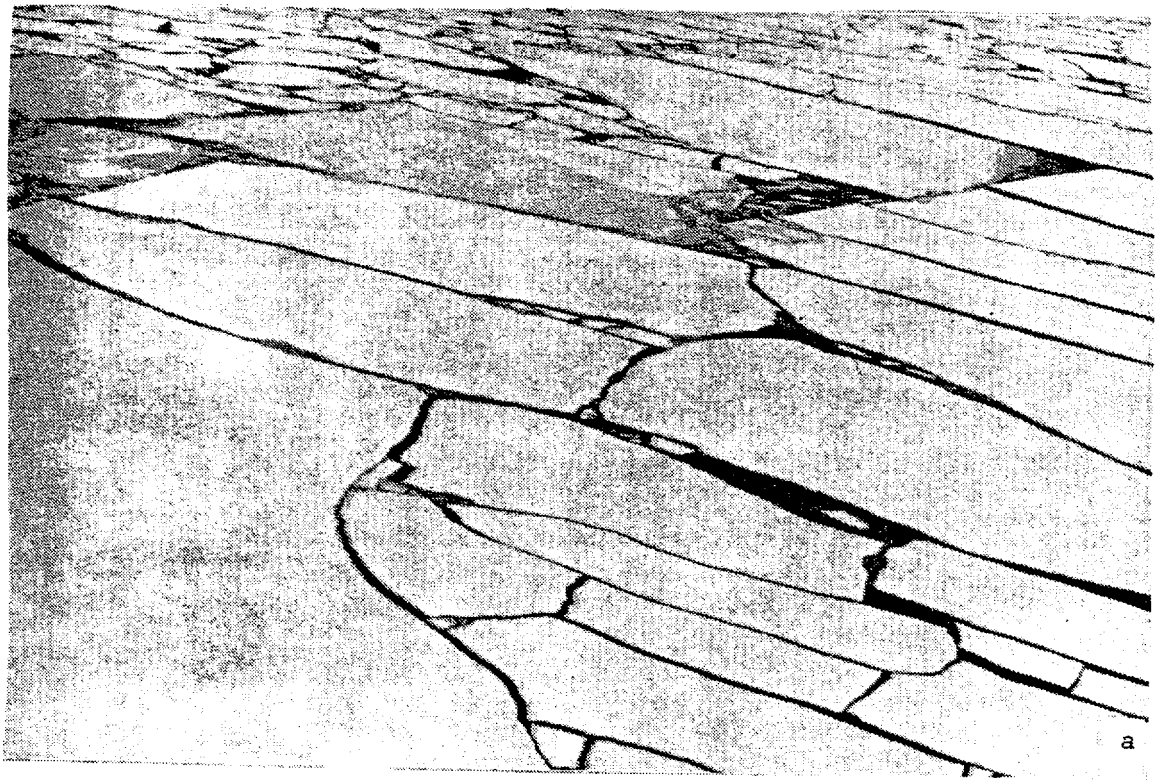

Figure 5. Floes in the transition zone on 9 March 1979 (day 68); (a) Aerial view from 150 m showing ocean swell fracturing large floe into small floes measuring 20 m across. (b) Surface view, where helicopter is on the large floe in lower left of (a). Its thickness is 0.33 m.

our three traverses, where in each case the thickest ice occurred at the edge.

We also observed that during periods of off-ice winds, the transition between the open water and solid ice cover was complicated by the formation of ice edge bands. These long thin bands, which form from ice divergence, measured about 1 - 10 km in length and 0.1 - 1 km in width, were oriented perpendicular to the wind direction, and moved away from the solid ice cover with a higher velocity than the interior pack. Figure 15a shows these bands streaming off south of the solid pack. Bauer and Martin (1980) show that these bands continue to move away from the pack until they melt in the surrounding warmer water. Therefore, the change from open water to solid ice in the Bering Sea is not abrupt, but rather is a gradual transition over about 50 km changing from open water to ice bands with a 10 - 20% large area concentration, into the edge zone which has 40 - 70% ice concentration, then into the higher concentration transition and interior zones.

2,4 The Tires Ice Charts

For comparison with the SMMR results, one of us (S.L.M.) prepared ice charts from the Tires images (see Figures 8a, 14, 15a, and 17a for examples). To avoid bias, the ice charts (Figures 8b, 11, 15b, and 17b) were prepared independently and without knowledge of the SMMR charts.

The Tires imagery, which is available in both the visible and infra red wavelengths, has two problems. First, clouds frequently obscured the image; second, the satellite orbit often produced extremely oblique images. Because both these factors prohibited daily coverage of the Bering Sea, when coverage was not available we extrapolated the ice cover from a combination of previous or subsequent images. To transfer

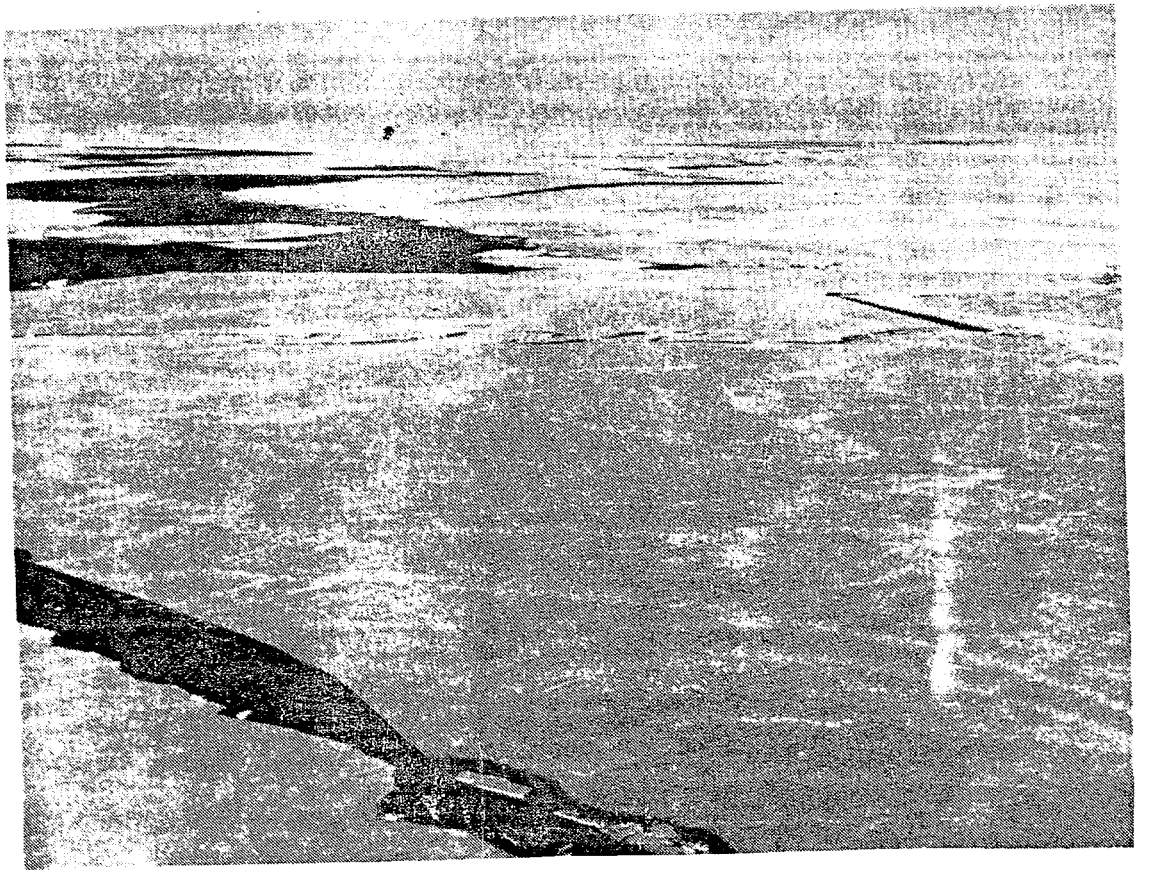

Figure 6. Aerial view of large ice floes in the interior zone from 150 m on 6 March 1979 (day 65). Ice thickness is 0.24 m.

the Tires data to a standard map base, we used a Zoom Transfer Scope. (ZTS) . The ZTS permits correction of the image distortion and the hand drawn transfer of the adjusted image to a base map. In this transfer, the resolution and scale of the original image limits the practicability of gaining information from the enlarged image. The location of land areas gives the best geometric control, so that our data plots are on a small-scale polar stereographic projection. Comparisons with Landsat imagery show that the error induced is in the rotational shift of the location of a feature and not in its shape or area (McNutt, 1981) .

On the charts we classify the ice in terms of both ice type and concentration. The different shadings on the ice chart divide the ice into the six categories of fast ice, new-young ice, first year-young ice, medium first year ice, thick first year ice, and the diffuse ice bands at the edge. These qualitative ice types do not imply an ice thickness; the identification is made in terms of the gray scale on each image. Second, ice concentration is expressed in terms of percentages, which are expressed to an accuracy of 25%. The cause of this low accuracy is the small scale of the Tires image and the presence of low clouds over the ice, in particular over open water regions.

In summary, the accuracy of the charts depends on the clarity of the original image, the amount of cloud cover, and the distortion inherent in the satellite photo. Since the locational error increases away from land, the most accurate portions of these images occur near land.

3. THE SMMR IMAGERY

3.1 SMMR Radiances

The study of sea ice by means of microwave remote sensing from space has evolved from the use of the single wavelength measurements of the Electrically Scanning Microwave Radiometer (ESMR) aboard Nimbus-5 [Gloersen et al. (1974), Zwally & Gloersen (1977), and Gloersen et al. (1978)] to the multispectral measurements of the Scanning Multichannel Microwave Radiometer (SMMR) on Nimbus-7 [Gloersen & Barath (1977)]. The Nimbus-7 SMMR measures microwave radiances at five wavelengths (4.55, 2.81, 1.67, 1.43 and 0.81 cm) for both horizontal and vertical polarizations providing ten channels of radiometric brightness temperatures. The spatial resolution of the instrument as defined by the integrated field-of-view (FOV) ranges from 148 x 151 kilometers at 4.55 cm to 27 x 32 kilometers at 0.81 cm. Gloersen & Barath (1977) give a complete summary of the instrument operating characteristics.

The usefulness of microwave measurements results from the high contrast in emitted radiances between open ocean and sea ice. The microwave radiation can be expressed as a brightness temperature through the application of the Rayleigh-Jeans approximation and written as a product of emissivity and physical temperature. The brightness temperature within a spacecraft instrument FOV is a composite of contributions from the surface of the earth, the atmosphere, and reflected components at the surface of both the atmospheric radiation and free space radiation [Gloersen & Barath {1977)]. With the assumption that the contribution from both the atmospheric and space components are negligible, the brightness temperature, T_B, observed by the satellite is simply

$$T_B = eT_S, \qquad (1)$$

where e and T_S are respectively the emissivity and surface physical temperature.

In the discussion to follow the sea surface will be considered either to be ice free, open ocean or to be covered only by first-year ice corresponding to the Bering Sea. Finer distinctions of ice type, as for example, new, young, and thin first-year ice, are not made since discrimination between thin ice and water within a given FOV of the instrument remains ambiguous. Figure 7a presents typical emissivity values for both calm open ocean and first-year sea ice at each of the SMMR wavelengths and polarizations. The calm open ocean values are optical model results corresponding to a thermodynamic temperature of 271 K while the ice emissivities are derived from observed Nimbus-7 SMMR brightness temperatures and physical surface temperature measurements made during nearly-coincident aircraft flights over first-year ice in Baffin Bay. The ice emissivities for both horizontal and vertical polarizations are greater than 0.9 at all wavelengths and exhibit little spectral variation. On the other hand, the water values are considerably lower, decrease with increasing wavelength, and have a much greater degree of polarization. Differences between vertical and horizontal ice emissivities range from 0.02 at 4.55 cm to 0.08 at 0.81 cm, whereas those for water fall within the range 0.26-0.29 at all wavelengths. This difference in the degree of polarization between water and ice is used below to retrieve ice concentration information.

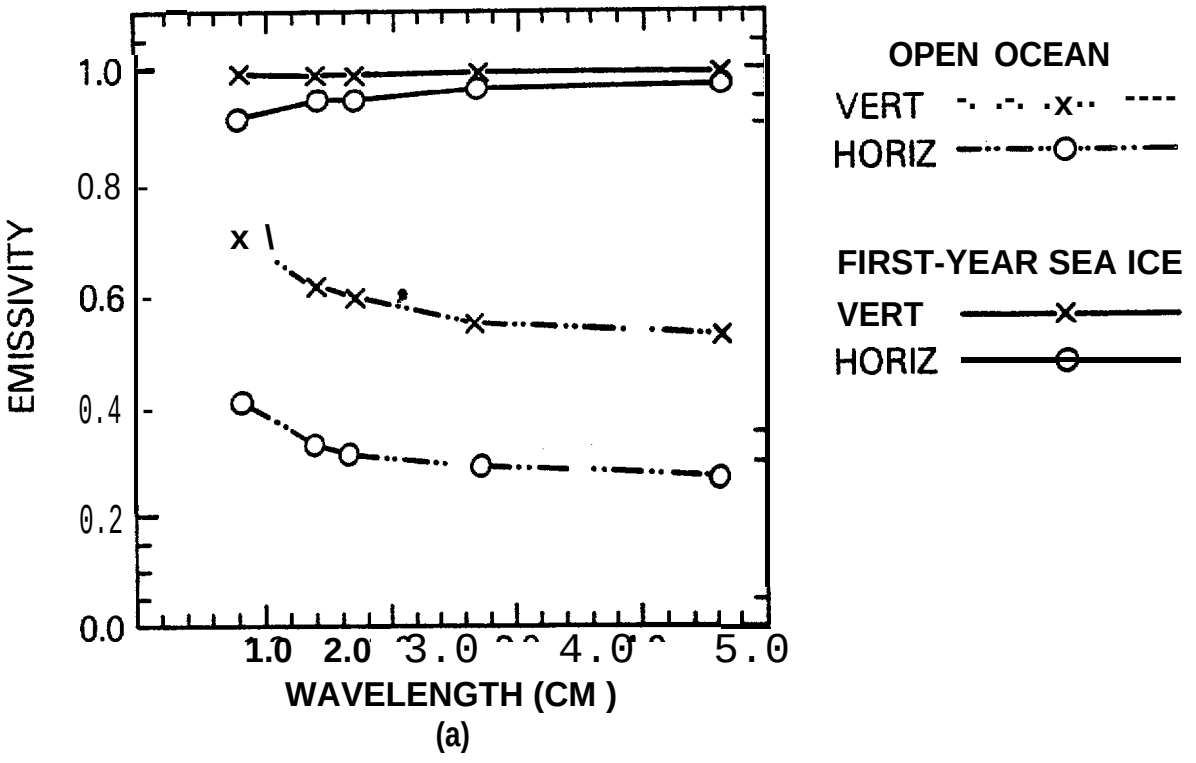

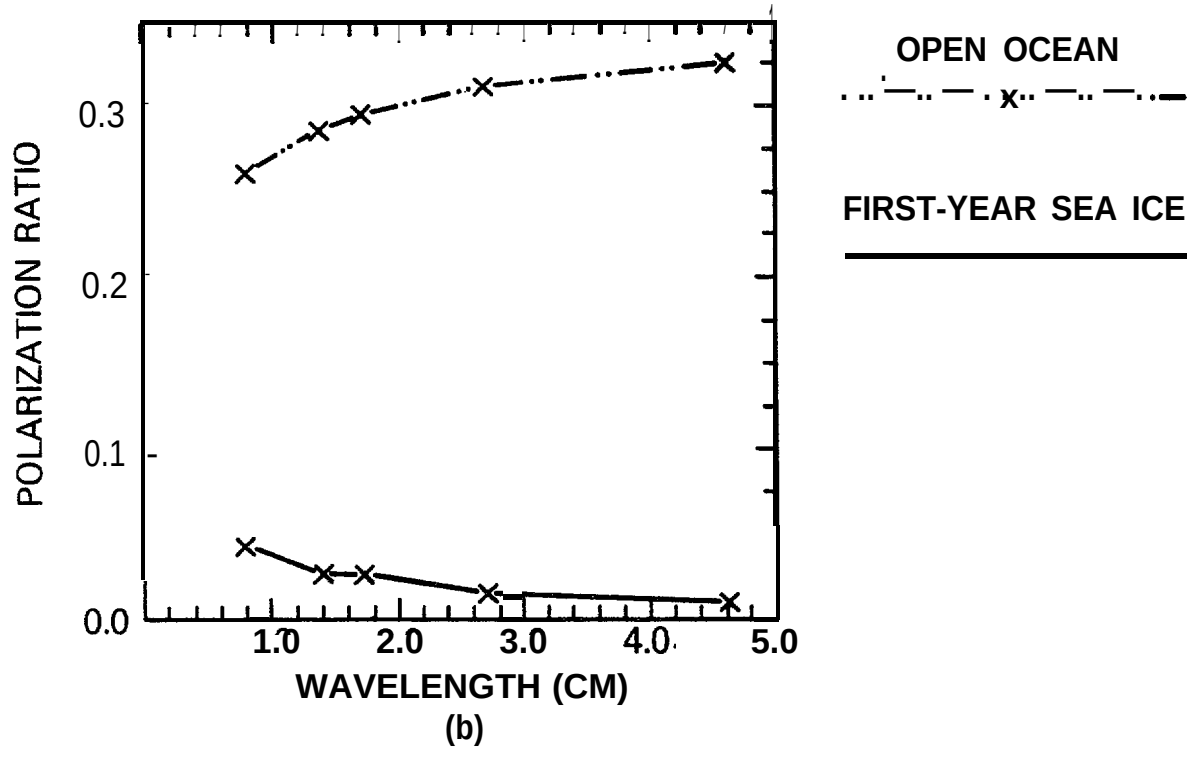

Figure 7. Microwave emissivities and polarization ratios at each SMMR wavelength for calm open ocean and first year sea ice. (a) Emissivity values. (b) Polarization ratios.

The polarization ratio PR, a measure of the degree of polarization, is defined in terms of observed SMMR brightness temperatures for a given wavelength as follows:

$$PR = \frac{T_B(vert) - T_B(horz)}{T_B(vert) + T_B(horz)} \quad , \qquad (2)$$

Figure 7b plots PR for each SMMR wavelength; the advantages of using this brightness temperature ratio are 1) the surface temperature dependency is largely removed and 2) any residual instrument gain variations will be reduced. From Figure 7b the difference between PR for water and ice varies from 0.32 at 4.55 cm to 0.22 at 0.81 cm. This large water-ice contrast and the near-independence of PR on physical temperature variations makes PR suitable for computing sea ice concentration.

3.2 Ice Algorithm

In the case when the instrument FOV is filled by a mixture of first-year ice and water, the surface emissivity is

$$e = e_w(1-C) + e_I C \quad , \qquad (3)$$

where e_w and e_I are the emissivities of water and ice respectively and C is the ice concentration, or the areal fraction of the field of view that is ice-covered. For this simple single ice species case, the brightness temperature equation becomes:

$$T_B = e_w T_w (1-C) + e_I T_I C \quad , \qquad (4)$$

where T_W and T_I represent the physical temperature of the sea surface and ice respectively. Our purpose here is to show that even with this crude model variations in ice cover are observed which, as will be seen below, agree well with analyses based on both visible satellite imagery and near-surface observations.

Equation (2) can now be used with the simplified expression for brightness temperature within an FOV [Equation (4)] to derive a relationship between C and PR for each of the five SMMR wavelengths. The resulting expression is

$$C = \frac{1}{1-R} \quad , \tag{5a}$$

where

$$R = \frac{T_{BI}(horz) - \left(\frac{1 - PR}{1 + PR}\right) T_{BI}(vert)}{T_{BW}(horz) - \left(\frac{1 - PR}{1 + PR}\right) T_{BW}(vert)} \tag{5b}$$

$T_{BI(horz)}$ and $T_{BI(vert)}$ are horizontal and vertical brightness temperatures of consolidated first-year ice and $T_{BW(horz)}$ and $T_{BW(vert)}$ are the corresponding brightness temperatures of calm open ocean. In equation (5b) we set the ice and water brightness temperature values to those observed in the Bering Sea. In this report, we use only the 0.81 cm channel to obtain the highest spatial resolution. For the 0.81 cm wavelength, these values are

$$T_{BI}(horz) = 215 \text{ K}, \qquad T_{BW}(horz) = 120 \text{ K},$$
$$T_{BI}(vert) = 242 \text{ K}, \qquad T_{BW}(vert) = 192 \text{ K}, \tag{6}$$

which were obtained from orbit 1966 (day 74:1202), an orbit coinciding with a period of relatively clear"' atmospheric conditions. This tuning of the algorithm was done in lieu of in situ Bering Sea measurements of ice emissivity and physical temperature on scales comparable to the SMMR FOV's. The polarization ratios derived from (6) differ slightly from those presented in Figure lb. The Bering Sea water ratio of 0.23 is 0.03 less than the model value for calm ocean (Figure 7b) indicating a wind roughened surface or an atmospheric effect or both. The Bering Sea first-year ice polarization ratio is 0.06 while that of Baffin Bay ice is 0.04 reflecting real differences in the physical properties of the ice as, for example, increased surface roughness which would tend to depolarize the received microwave radiances.

Equation (5) with the values from (6) is used to compute ice concentrations from the polarization ratios calculated from the observed SMMR brightness temperatures. Because the algorithm translates emissivity variations into concentration variations, the accuracy of the concentration retrievals depends primarily on the observed ice having an emissivity close to the tuned value. Since thin ice species have emissivities between those of open water and thick first-year ice, areas of thin ice translate into areas of lower ice concentration. As an example, actual radiance and sensible surface temperature measurements made during AIDJEX [Gloersen et al. (1978)] show that the emissivity differences between thick snow-covered first-year ice and thin ice without snow cover at 0.81 cm is 0.01 for the vertical polarization and 0.08 for the horizontal. In the algorithm, the ice concentration noise amplification factor for variations in ice emissivity is approximately 3, so that the error in ice concentration caused by an emissivity varia-

tion of 0.0S is approximately 15 percent. Therefore, based on the AIDJEX data, we expect for the Earing a maximum concentration error of up to 24 percent. Because of this limitation on accuracy, it is the relative position of high and low ice concentration regions and concentration gradients which are of prime importance. In. fact, we show In §4 that these features correspond well with patterns of thin and thick ice in the ice charts.

3.3 Spatial Resolution of Data

As previously mentioned, the FOV size of each SMMR channel decreases with decreasing wavelength. The FOV or footprint of the instrument is elliptical in shape with the long axis in the direction of spacecraft motion because of spatial smearing due to both the integration time and the spacecraft velocity. The 0.81 cm channel has the highest resolution, or an integrated FOV of approximately 27 x 32 kilometers. We use this channel below in the ice algorithm to obtain information on the smallest possible scale. The resolution has been degraded somewhat by "binning"' the brightness temperatures from each individual FOV into cells approximately 30 km x 30 km in order to accommodate existing software packages for producing the contour plots.

The maps on which the SMMR data have been contoured were generated from the Wolfplot package[1] of routines and have an accuracy of 0.1 degrees latitude (11 km) in both latitude and longitude. Examination of these maps shows, however, that landfall may be in error by as much as 0.2 degrees latitude. Part of this may be due to inaccuracies resulting from the plotting of the land boundaries themselves. In any case, the

[1]The Wolf Plotting and Contouring Package by G.T. Masaki 1972 (Revised Ed. 1976) Computer Sciences Corporation, Silver Spring, MD.

mapping errors are within the microwave resolution size and should not significantly affect the results of the comparison.

4. Comparison of Data

This section compares the surface, aircraft, and Tires data described in §2 with the SMMR algorithm results. Table 1 summarizes the data used in the comparison. Specifically, we examine in the following sub-sections the ice behavior for 3, 9, 15, and 25 March, and show that the SMMR algorithm gives a good description of both the ice edge and the observed ice interior properties.

4.1 3 March (day 62)

Figure 8a shows the Tires image, and 8b shows the ice chart prepared from 8a. Examination of these figures shows that the northeast winds shown on Figure 2a drove the ice away from the Alaska mainland, from the south coast of Nunivak, St. Lawrence, and St. Matthew Islands, and from the northern part of the Gulf of Anadyr, thus creating lee-shore regions of both thin ice and low ice concentrations. The southwest advection of ice is also responsible for the thick ice plume of ice extending southwest from Norton Sound to the ice edge, and for the high concentration region in the southern Gulf of Anadyr.

For comparison with the ice chart and aircraft and helicopter data, Figure 9 shows the SMMR ice concentration chart. On the chart we plot contours of constant ice concentration at intervals of 10% up to 95%. To simplify the presentation and to minimize the effects of roughened seas and atmospheric liquid water, the lowest concentration shown is 25%. On the chart, the solid white line is the P-3 ice edge, the symbols S1 and S2 show our helicopter core locations, and the letters "A-F" show regions of comparison with the Tires ice chart. As Table 1 shows,

Table 1. Summary of the research platforms and the times of their observations

Mode	Orbit	Julian Day	GMT
3 March			
Tires		62	0020
Helicopter		62	00-02
P-3		62	00-03
SMMR	1806	62	2202
9 March			
P-3		68	00-03
HELO		68	18-21
SMMR	1889	68	2202
Tires		(average of day 67, 69)	
15 March			
HELO		74	00-01
SMMR	1966	74	1202
Tires		75	0127
25 March			
SMMR	2110	84	2149
Tires		85	0124

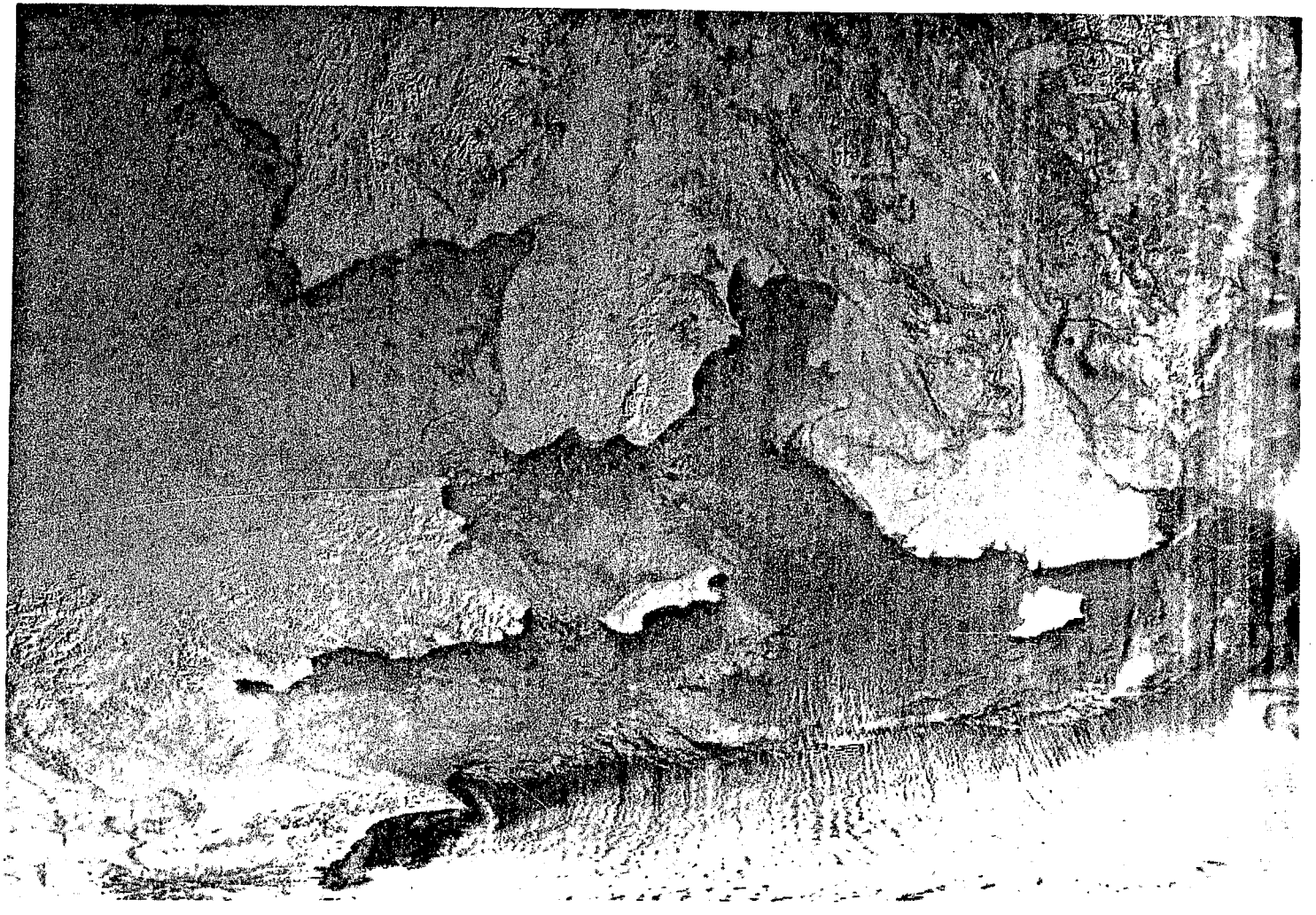

Figure 8a. Tires image for 3 March (62:0020); see text for further description.

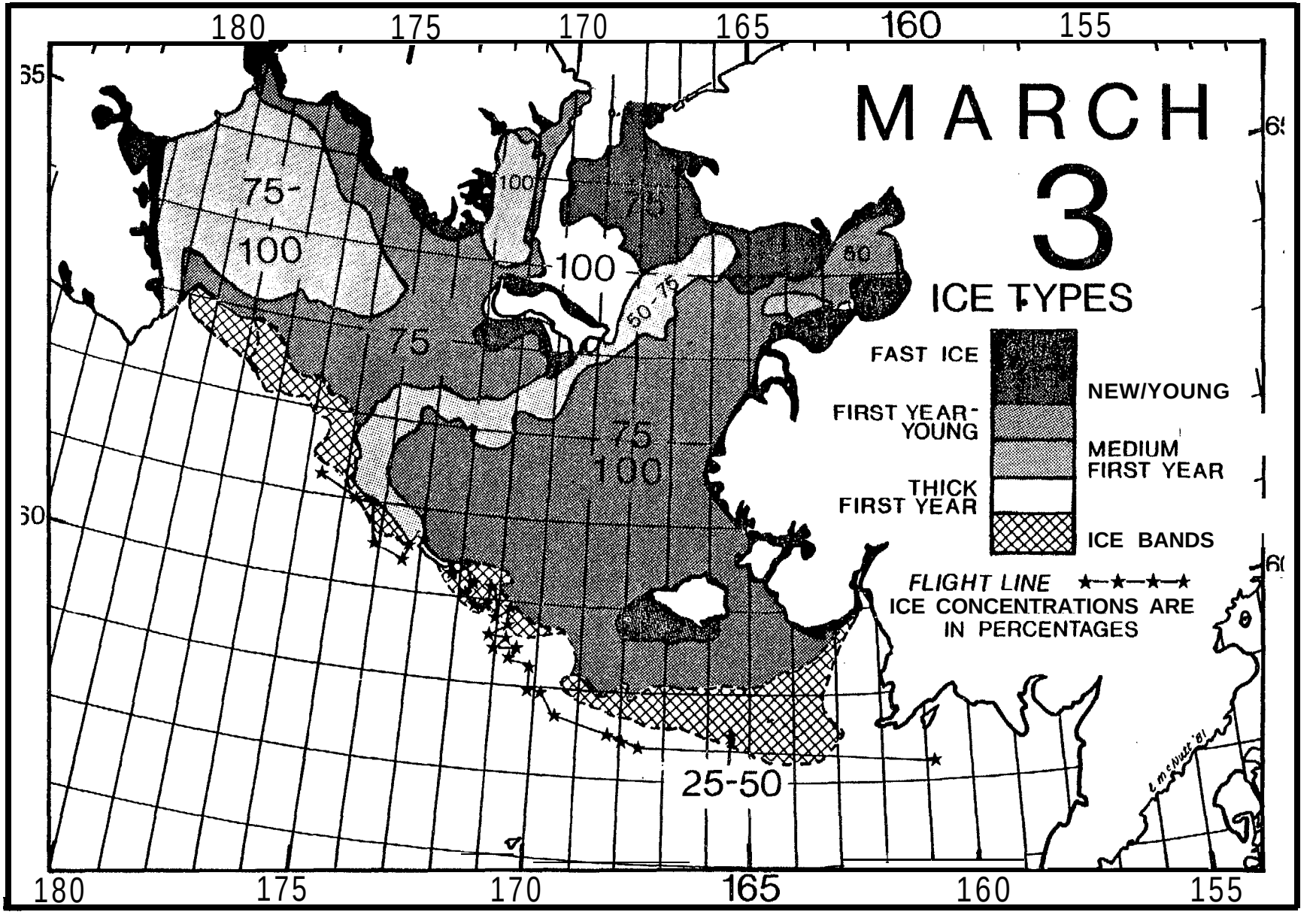

Figure 8b. Ice chart derived from Figure 8a.

the data used in the comparison was taken about 20 hr before the SMMR image.

Examination of Figure 9 shows that the ice edge is defined by a concentration gradient ranging from 25 to 55% over a distance of about 50 km. The cause of this 50 km width is partly the SMMR FOV, and partly the width of the physical transition from open water to the ice interior described in §2.2. Along this gradient region, the white line shows the P-3 ice edge position, where Appendix A gives a copy of the reconnaissance report. Because the ice observer took this line in part from a classified radar, we are unable to check independently the ice position; however, examination of the figure shows that the line lies within 1/4" latitude of the SMMR edge, or within one SMMR cell.

Second, the two points S1 and S2 lying below Nunivak Island show the location of the ice cores taken by helicopter. Figure 10a shows an aerial view of the field of 10 m diameter floes from which core S2 was taken and 10b shows a surface view. We measured this floe thickness as 0.80 m; the ice appearance in the photograph is similar to that at S1 where we measured a 0.60 m floe thickness. From the pictures, the ice at S1 and S2 consists of small thick floes, floating in a layer of about 0.1 m thick grey ice. Examination of our photographs from this region supports the algorithm result of a 50-60% concentration.

Finally, the letters on Figure 9 mark regions of comparison between the SMMR data, the ice chart, and the Tires image. First, "'A" marks the broad region of young uniform ice filling the eastern Bering Sea. As we expect from the predominantly northeast winds, the concentration decreases toward the Alaskan coast. Also, the 65% contour to the left of "A'* outlines approximately the boundary between the young and medium

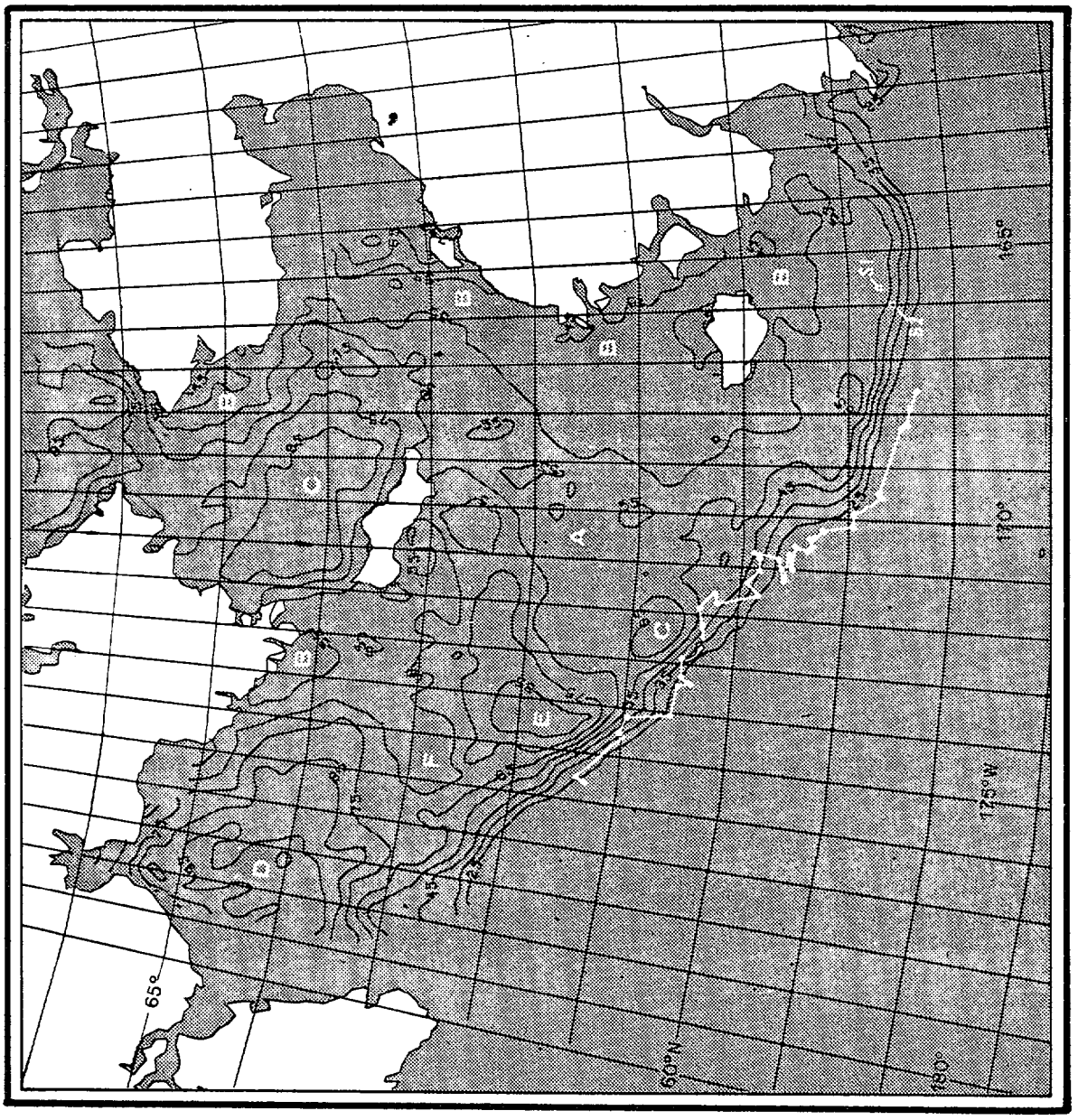

Figure 9. The SMMR ice chart showing contours of ice concentration in intervals of 10% computed from the 0,81 cm wavelength for day 62:2200. See text for further description.

first year ice shown on the ice chart. There is a discrepancy in concentration, however, between 45-65% ice concentrations in the region marked by "A", and the 75-100% concentrations in the same region on the ice chart.

The cause of part of this discrepancy may have occurred in the transfer of the ice concentration data from the Tires image to the ice chart. With thin or medium first-year ice appearing dark grey on the image, thicker ice as white, and open water as black, to the ice observer open water shows up better in white ice than in dark grey ice, so that the thin ice concentration can be easily overestimated. The second cause of this discrepancy, as Section 3.2 discusses, is that for the same concentration of thin and thick ice, the present algorithm shows the thin ice as having a lower concentration than thick ice. We suspect that a combination of ice observer and algorithm error causes the above discrepancy.

To continue with the letters on the chart, the regions "B'" show the coastal ice-generation regions, which are physically characterized by both thin ice and low concentrations. Because of land contamination in the algorithm, the contouring for these regions breaks down within a SMMR FOV or approximately 1/4° latitude of land. Next, the "C's" mark the regions of thick ice and high concentration to the north of St. Lawrence and to a lesser degree north of St. Matthew Island, where the winds drive the ice against the coasts. The concentration decrease immediately north of both islands is again caused by land contamination. Fourth, in good agreement with the ice chart, "D" marks the region of older, thicker ice in the Gulf of Anadyr.

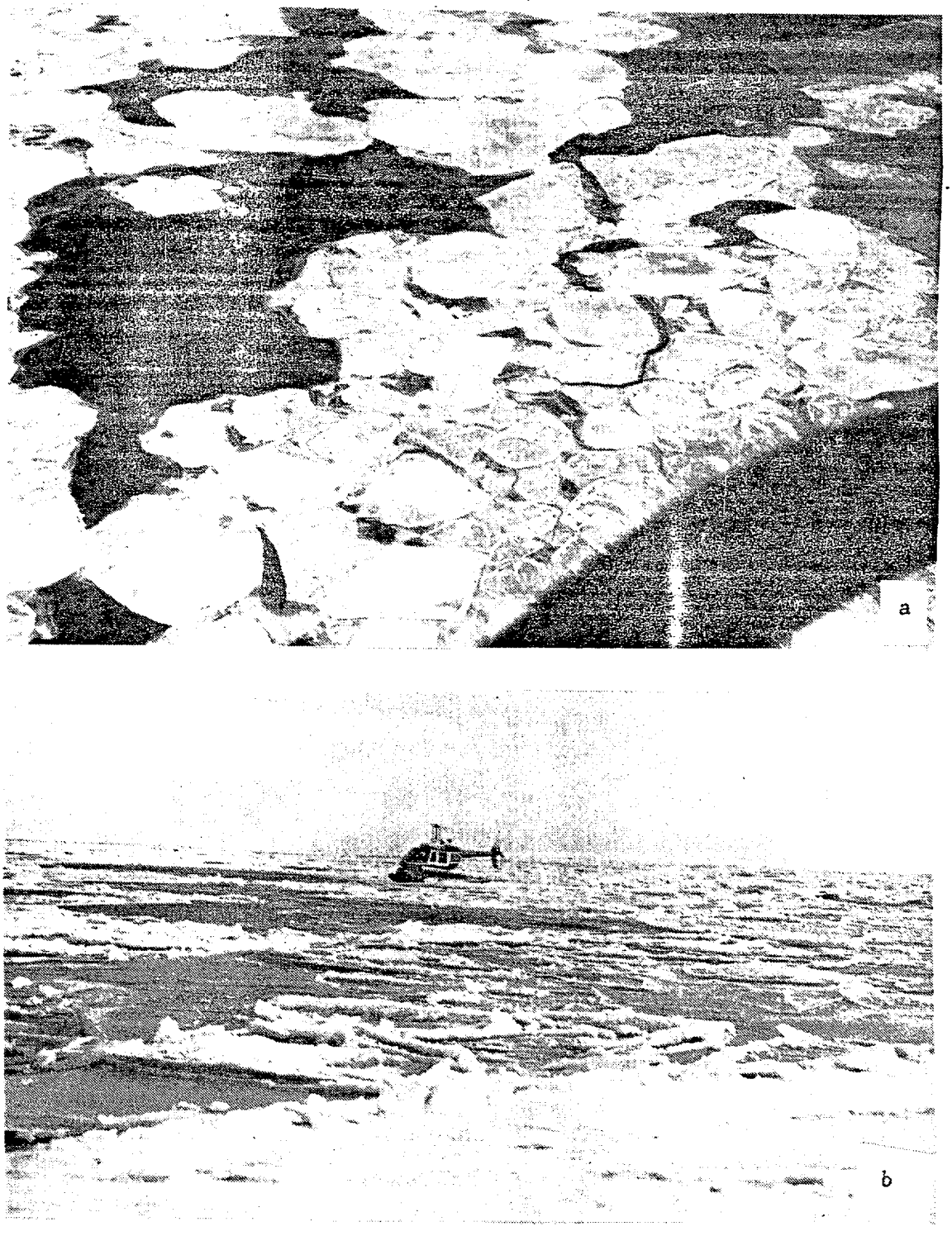

Figure 10. Aerial and surface view of site S2. (a) Aerial view from about 150 m; floe S2 is white floe at lower left measuring about 10 m across and 0.8 m thick. (b) Surface view of area from S2-showing 0.2 m thick grey ice beyond S2.

Fifth, "E" marks the region of older, thicker ice clearly shown on the Tires image and with a SMMR concentration of 65-85% and an ice chart concentration of 50-75%, where this-ice was probably advected down to the edge from Norton Sound. Finally, "F" marks the region of younger thinner ice in the western Bering Sea, which was generated both south of St. Lawrence and in the Gulf of Anadyr. Again for this case, the SMMR and ice chart concentrations agree.

In summary, comparison of the ice and SMMR charts show that the SMMR output gives good results for first, the ice edge; second, the low concentration, thin ice regions adjacent to the coasts; and third, the high concentration regions north of the islands, in the Gulf of Anadyr, and the plume center "E". The ambiguities in the algorithm results, which may be caused by errors in reading the Tires ice concentrations, occur in discrimination of the thin ice concentrations. We feel, however, that comparison of the two methods shows that, except within 1/4° latitude of land, the SMMR ice algorithm gives as good results as the ice chart in the interior, and a better definition of the ice edge.

4.2 9 March (day 68)

Between day 62 and 68, the Siberian high pressure system continued to dominate the weather so that as Figure 2b shows, the winds continued out of the northeast. Because of problems with clouds, we prepared the ice chart for this day (Figure 11) from an average of Tires images on days 67 and 69.

In addition to the ice chart, Table 1 shows that we also had a helicopter ice survey and a P-3 overflight preceding the SMMR image, where the P-3 preceded the SMMR by about 20 hr, while the ice survey was nearly simultaneous. Examination of the Tires ice chart, on which we

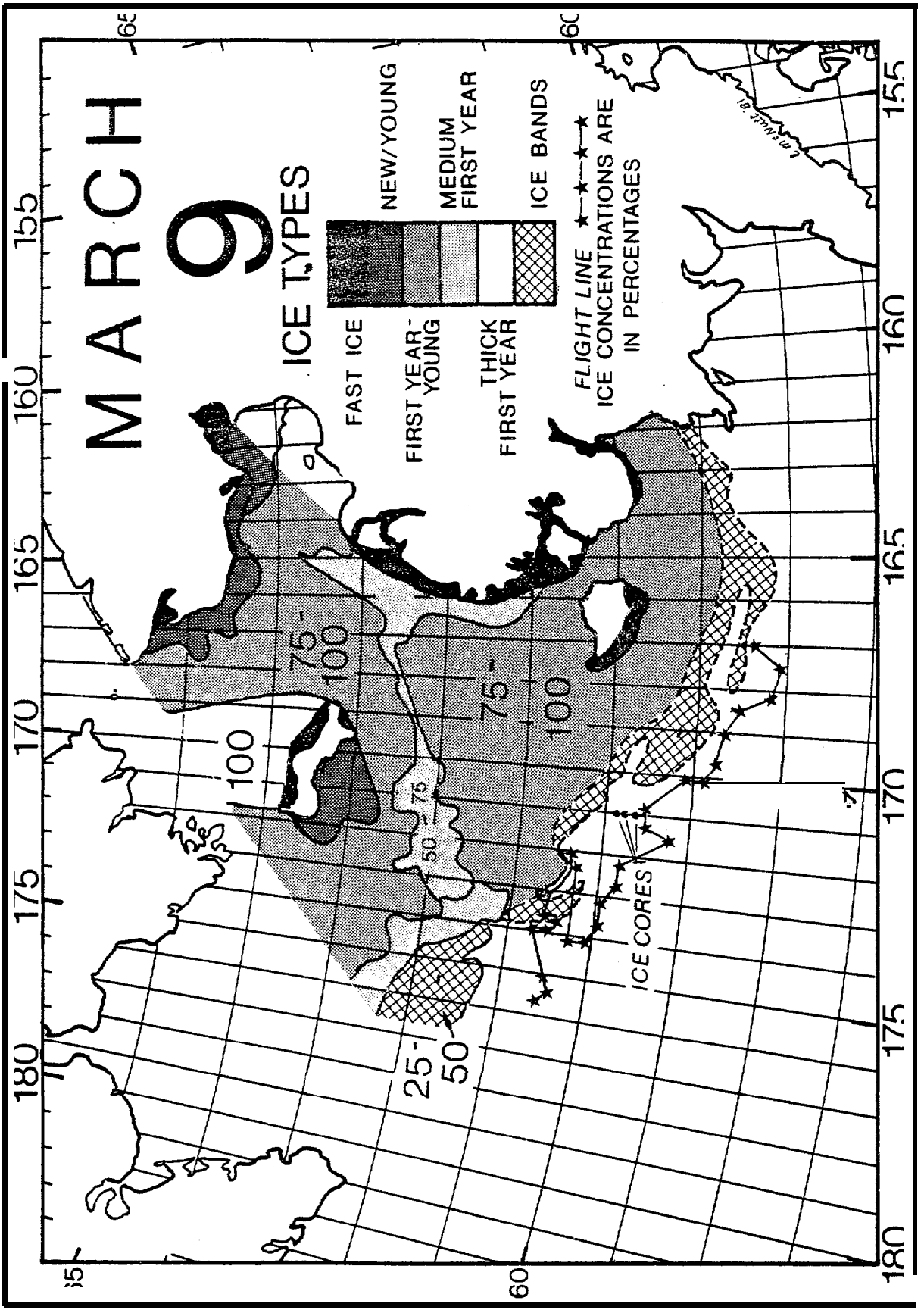

Figure 11. Ice chart for 9 March 1979 from Tires images on day 67 and 69. See text for further description.

plot the aircraft ice edge and ice core positions, clearly shows that the ice chart and the physical ice edge do not agree. The ice chart shows, however, many of the same physical features described for 3 March, specifically the thin ice and low concentration regions southwest of the coasts and islands.

For comparison, Figure 12 shows the SMMR ice concentration plot. On this figure, the solid white lines show the aircraft flight lines from Appendix B; one at the ice edge, and another in the ice interior northwest of St. Matthew Island. The figure shows that except in the immediate vicinity of St. Matthew Island, the P-3 ice edge is well correlated with the SMMR ice edge. The interior line, following and paraphrasing slightly the P-3 report, marks the "vicinity of the heaviest, thickest ice,'* and the circle marks the regions of "greatest concentration within a 10 nm radius'". Although the circle is not identified with any particular concentration feature, the interior track line follows the 85-95% concentration lines. Again the aircraft and SMMR results are in good agreement.

Second, the point C shows the ship location,,and C1-C4 show the line along which we took four ice cores. Along this line, Martin & Kauffman (1979) reported that the sky was heavily overcast, while the P-3 (Appendix B) also reported "undercast between 169.5°W and 171.75°W". The figure shows that, in spite of the overcast, the traverse line lies across both the SMMR and physical ice edge. Figure 13 shows a schematic of the ice concentrations and types observed along this traverse, and Figure 5 shows station C3. From Martin & Kauffman (1979) the ice thicknesses along this line are as follows: Cl is 0.25 m thick, C2 is 0.33 m thick, C3 is 0.33 m thick, and C4 is 0.15 m thick. Further, from our

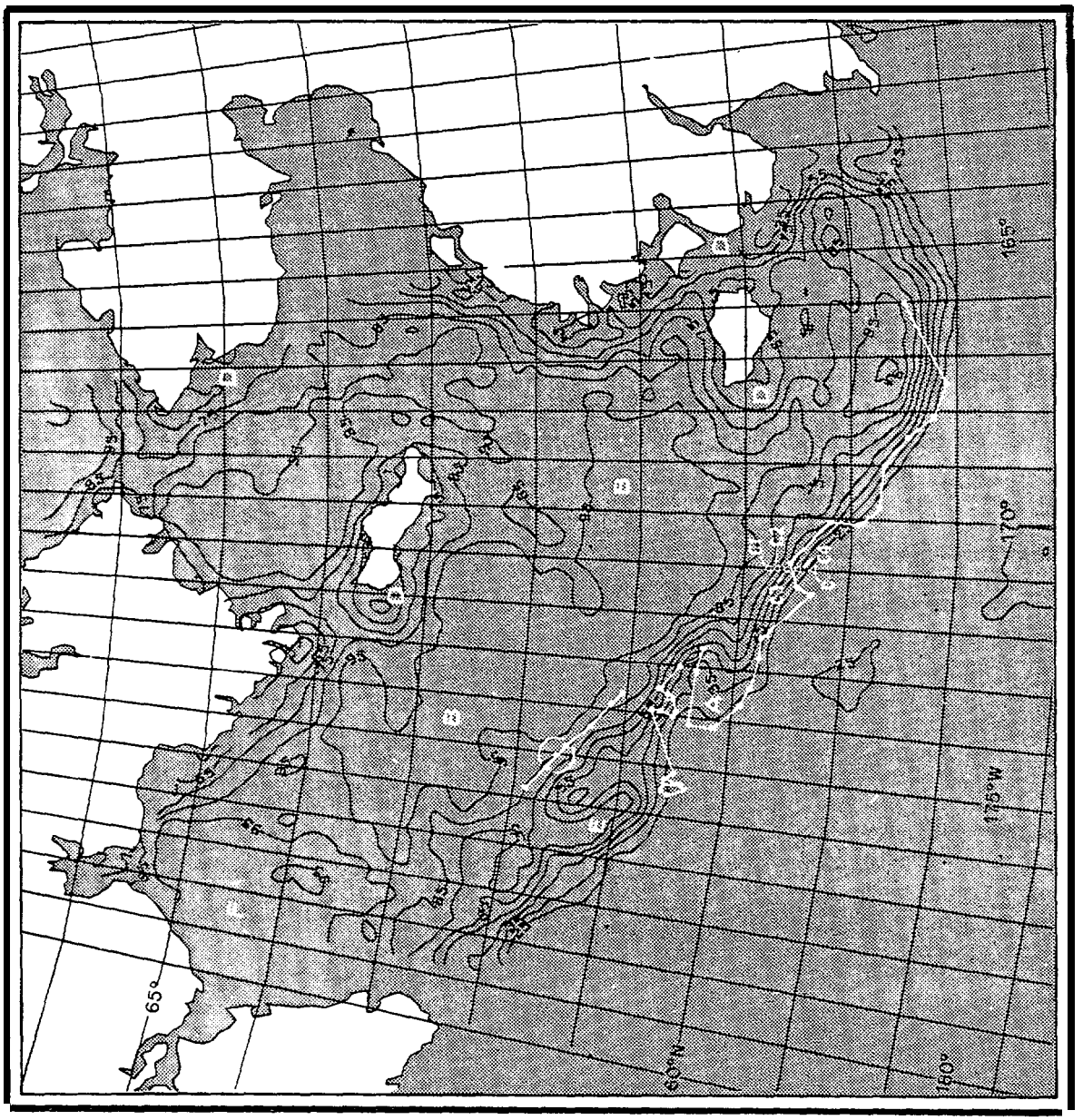

Figure 12. SMMR ice chart for 9 March (68:2200). See text for further description.

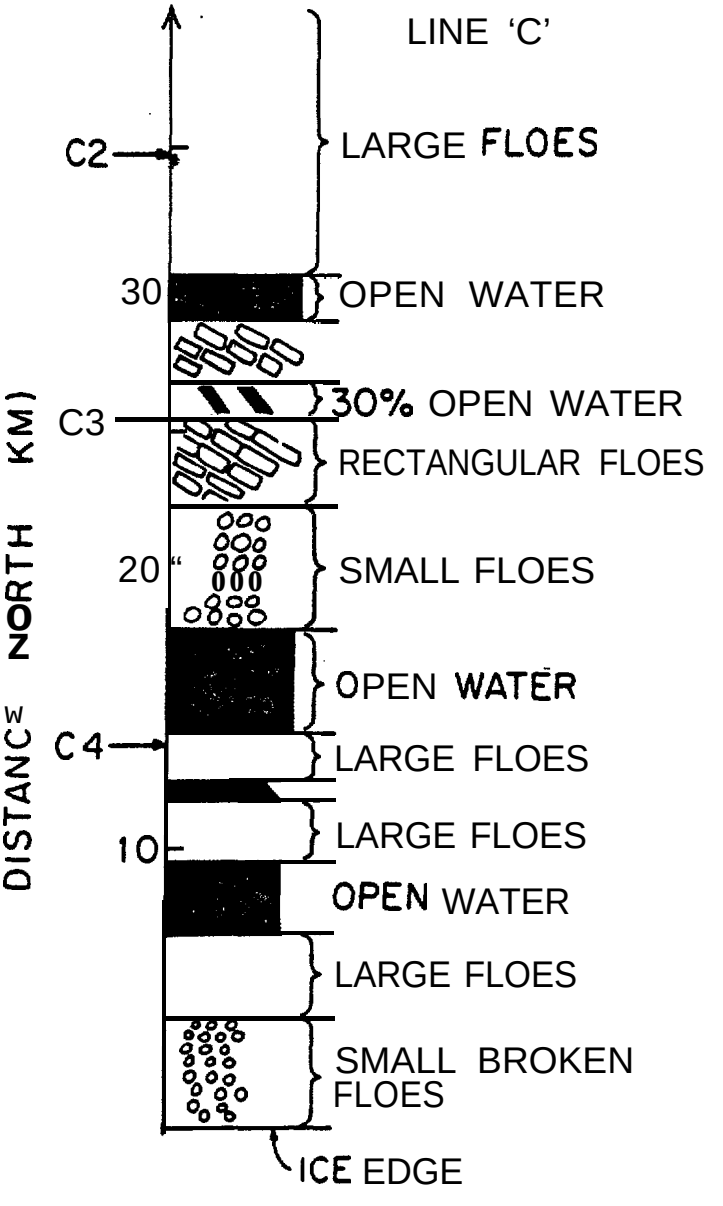

Figure 13. A diagram of the ice types along Line C [from Bauer & Martin (1980)]. Region above C3 marked "30% open water" consists of large floes in 30% open water; conditions at Cl (not shown) are similar to those at C2.

previous days' work from the ship, the small broken floes near the edge had thicknesses of 1-5 m. This complicated mixture of small broken floes, open water, and very large floes is a specific example of a traverse line in the ice transition region.

The capital letters on the SMMR chart again mark regions of comparison with the ice chart. "A'" shows the open water southwest of St. Matthew Island, which is marked by a dip toward the island of the concentration lines. The cause of the lack of agreement between this dip and the aircraft line may be the time difference between the two observations. "B'* marks the broad interior regions of high concentration, "D" the regions of new ice production southwest of the coasts and islands, and "F'" the high concentration region in the Gulf of Anadyr. These regions are in general agreement with the ice chart. Finally, the letter "E", which marks a feature not shown on the ice chart, is a local high concentration region, separated from the main pack by a low. To show that this local high probably represents a physical feature rather than a computer artifact, Figure 14 shows the closest clear 'Tires image of this region at day 66:0119, or almost three days before the SMMR image. The white arrow points to a large ice mass west of St. Matthew Island which is slightly separated from the main pack. This ice mass, which may be the advection southwest of the high-concentration feature also marked by 'SE" on Figure 9 at day 62, is probably the cause of the feature "E"' on Figure 12.

4.3 15 March (day 74, 75)

As the weather charts in Section 2.1 show, between day 68 and 74 the winds continued out of the northeast. Figure 15a shows the Tires image for day 75:0127, and Figure 15b shows the resultant ice chart. On

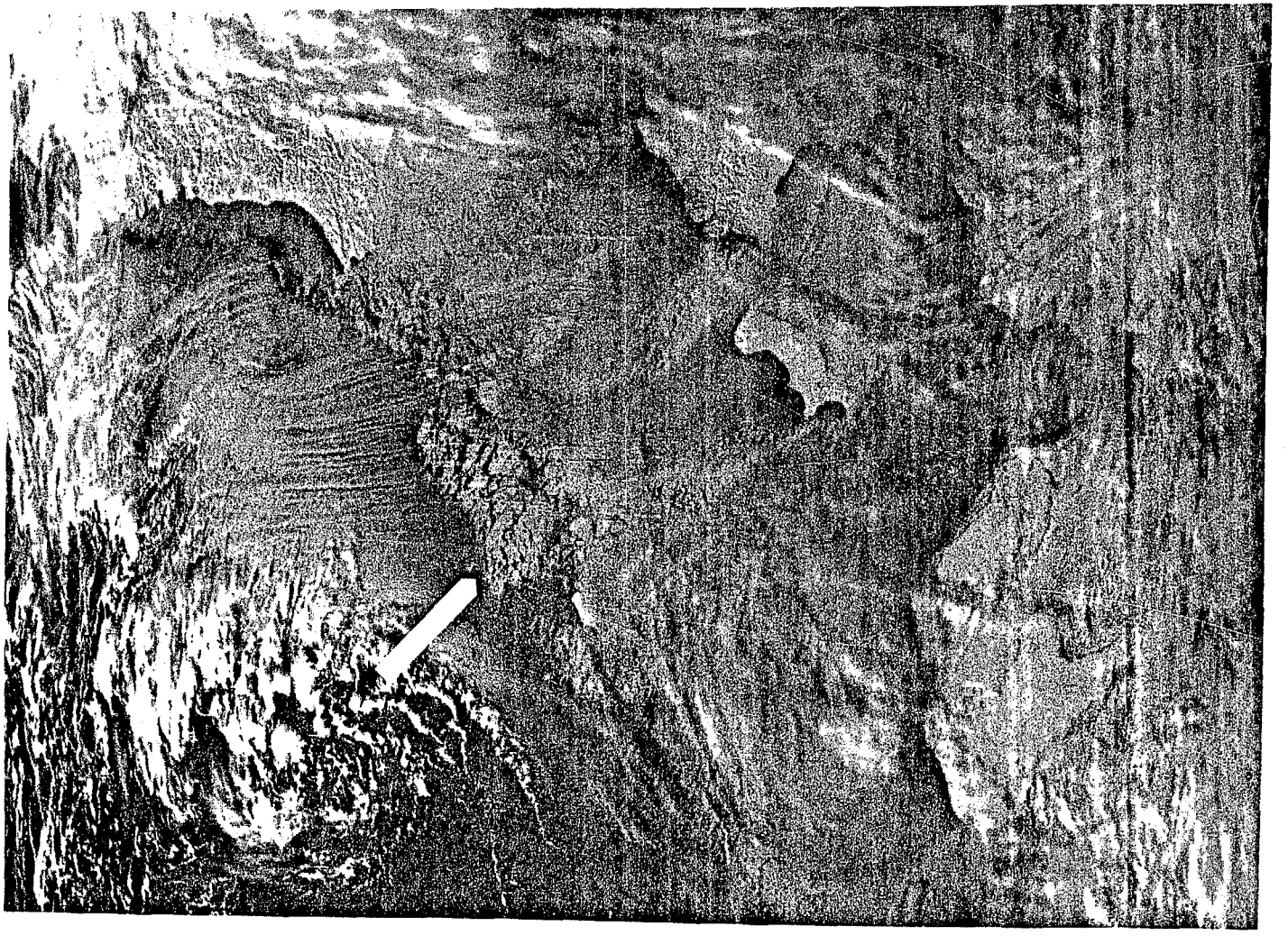

Figure 1⊏. Tiros i for day 66 O119; ωhite arrow poin⊏s to large detached ice mass.

the Tires image to the west of St . Matthew Island there is a cloud line over the ice parallel to the edge where the cloud shadow is visible on the ice cover. Comparison of these two images again shows the difficulty of making concentration estimates from the Tires images. On Figure 15b the ice tongue to the east of Nunivak Island was mapped from the day 73 Tires image. Figures 15a and b show that the ice is again characterized by thin ice and low concentration regions southwest of the major landmasses.

Figure 16 shows the SMMR ice chart for day 74:1202, where the letters N1,N2 show our core positions, and the other letters refer to significant ice features. For this case the SMMR swath covered only the eastern Bering Sea. The SMMR image again shows that the ice edge gradient region goes from 25% to 65-75% over approximately 50 km, again in agreement with the diffuse nature of the ice edge shown on the Tires image.

To discuss next the regions marked by capital letters on the SMMR image, ‘*A” marks the dip in the concentration lines caused by the polynya southwest of St. Matthew Island, and “B”’ marks the region of low ice concentration associated with the polynya southwest of St. Lawrence Island. In the Ice interior the “C’s’* mark the high concentration, broad region of thick and medium first-year ice shown on the ice chart, although comparison with the chart suggests that the concentration at the “C” immediately to the west of Nunivak Island is too large by 20%. "D" marks the low ice concentration region southwest of Nunivak Island, where a lower 65% concentration corridor extending from the Island to the ice edge separates the high concentration regions “E” and “C”. This low concentration corridor is clearly visible on both the ice chart and the satellite photograph.

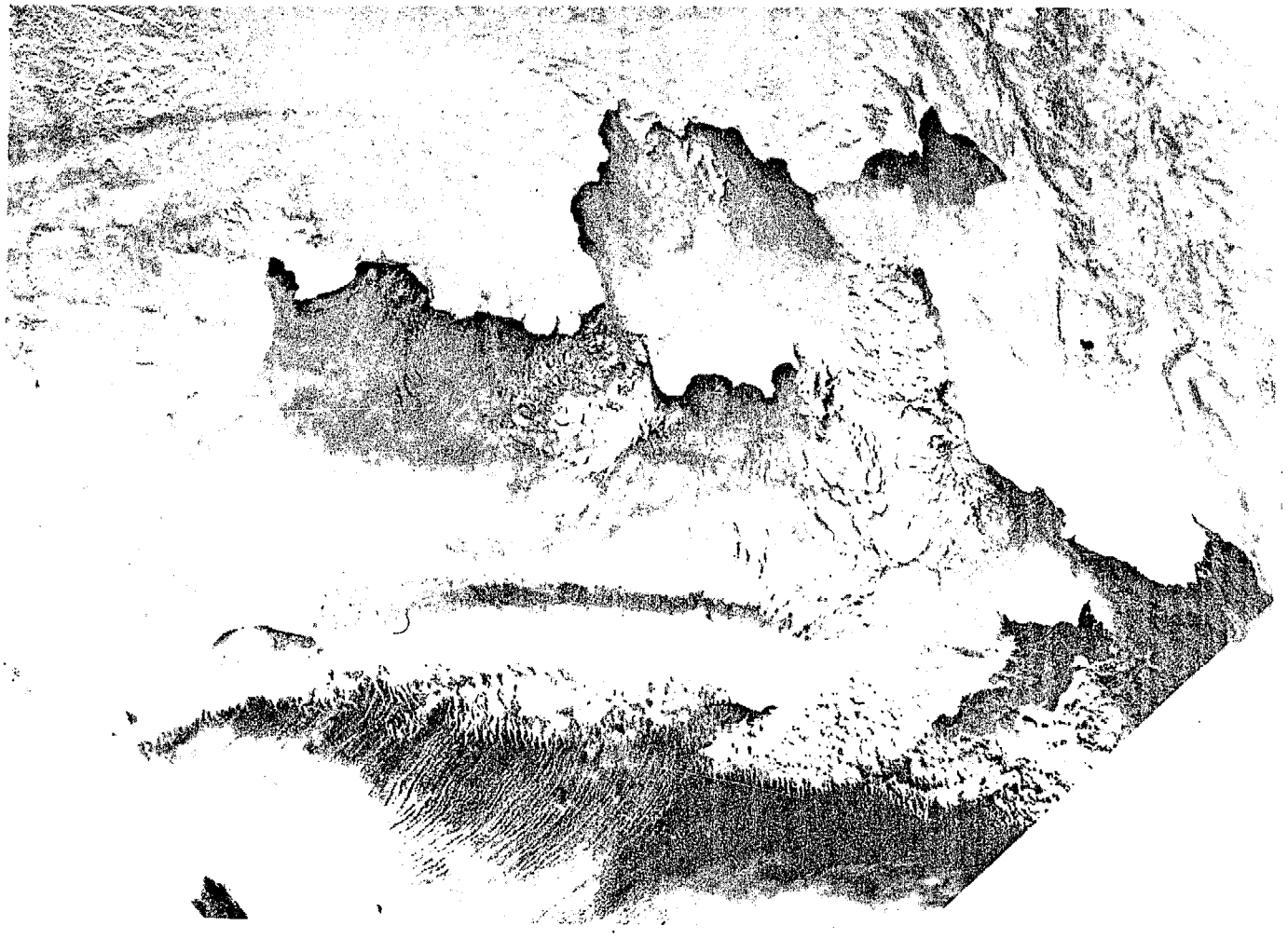

Figure 15a. Tires image for 15 March (75:0127).

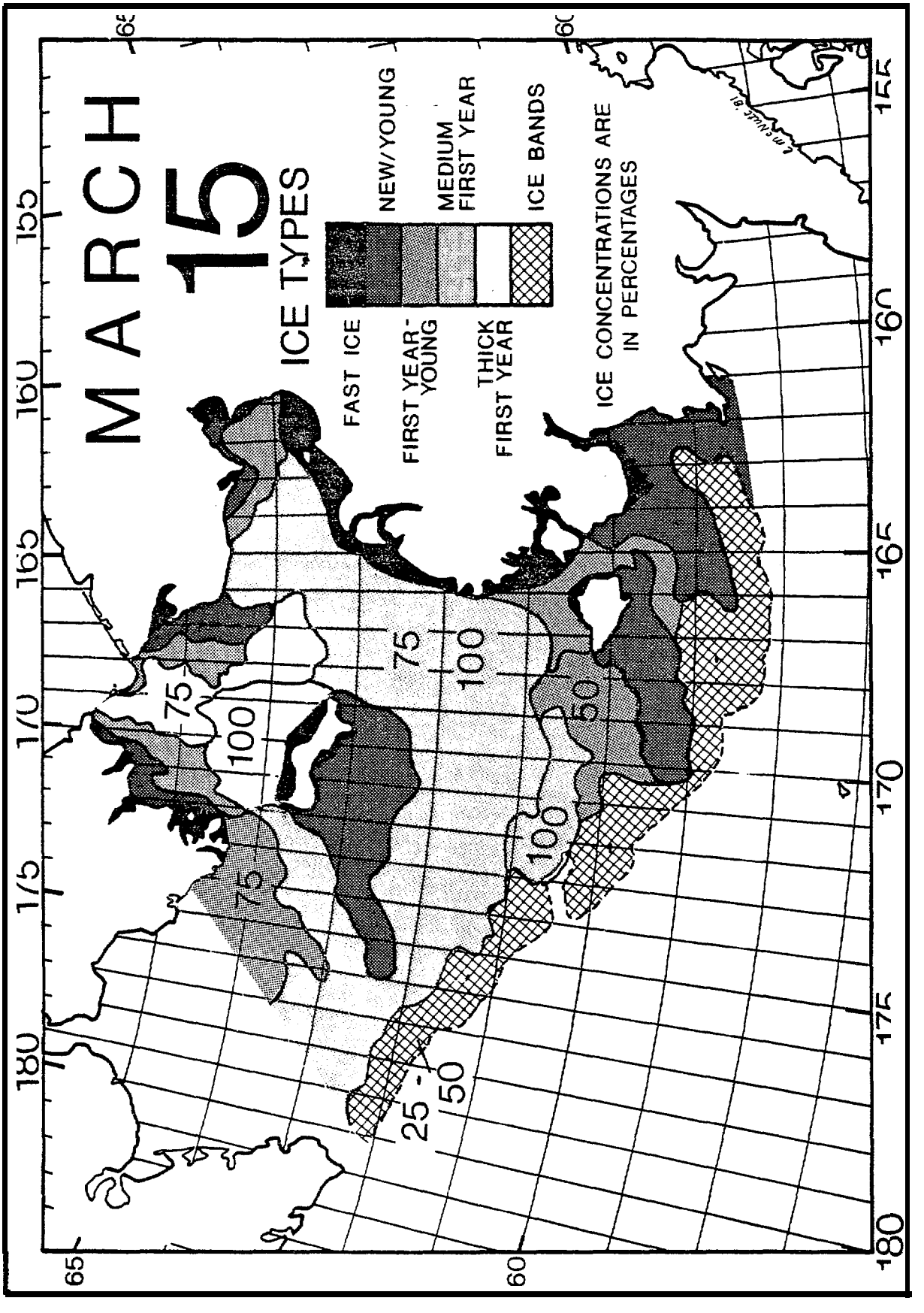

Figure 15b. Ice chart derived from Figure 15a.

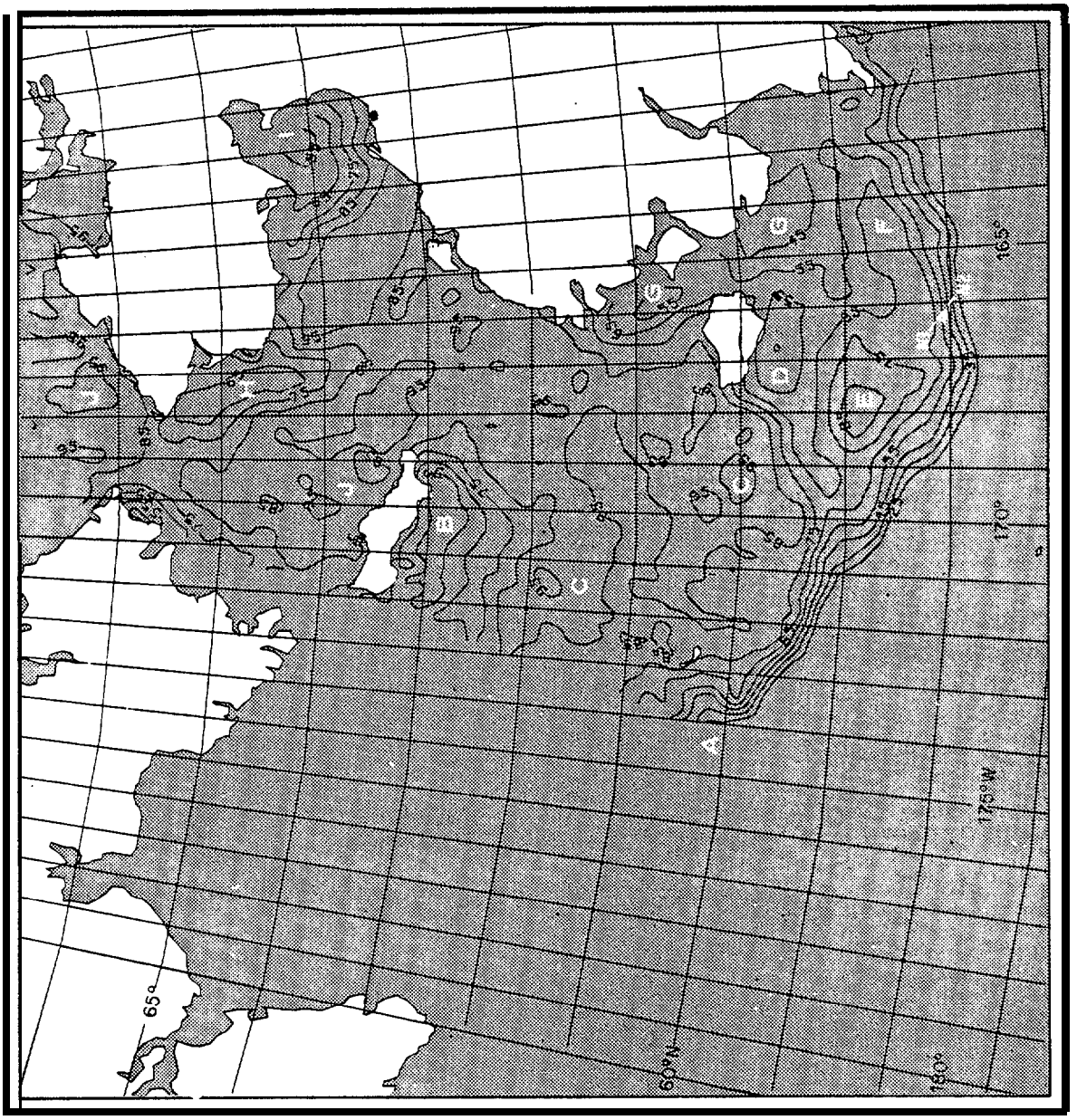

Figure 16. SMMR ice chart for 15 March (74:1202). See text for further description.

To the east of Nunivak Island, "F" marks the ice tongue that extends over into Kuskokwim Bay, and "G" marks the low concentration regions adjacent to the coast. Finally, in the northern Bering Sea, "H" and "I" respectively mark the low ice concentration regions off Cape Prince of Wales and in Norton Bay. Also north of both St. Lawrence Island and the Bering Strait, the 85-95% ice concentrations marked by '*Jts" show the wind-driven ice pile-ups.

Finally, the "N1" and "N2" which lie on the 55% contour line mark the core locations described in Martin & Kauffman (1979). From" our helicopter overflights, the ice in this region was diffuse and divergent. The floes were generally broken, with diameters of 20-100 m and with little pressure ridging. The ice consisted of a mixture of two broad types: grey-white ice with a 0.2 m thickness, and white ice with a 0.6 m thickness. From our aerial photographs we estimate the ice concentration here at 60%, which is consistent with the SMMR results.

4.4 25 March (day 74)

As section 2.1 describes, beginning 20 March a large low pressure system in the southern Bering Sea caused a weather pattern shift from cold northeast to warm southerly winds (Figure 2d). Because of this change, the Tires imagery from 20 to 25 March showed only clouds. Figure 17a (75:0124) shows the first clear image of the ice during this weather condition. Figure 17a and the derived ice map in Figure 17b show that the warm southerly winds during this period caused a large melt-back of the sea ice, so that an open water region now extends almost into Norton Sound.

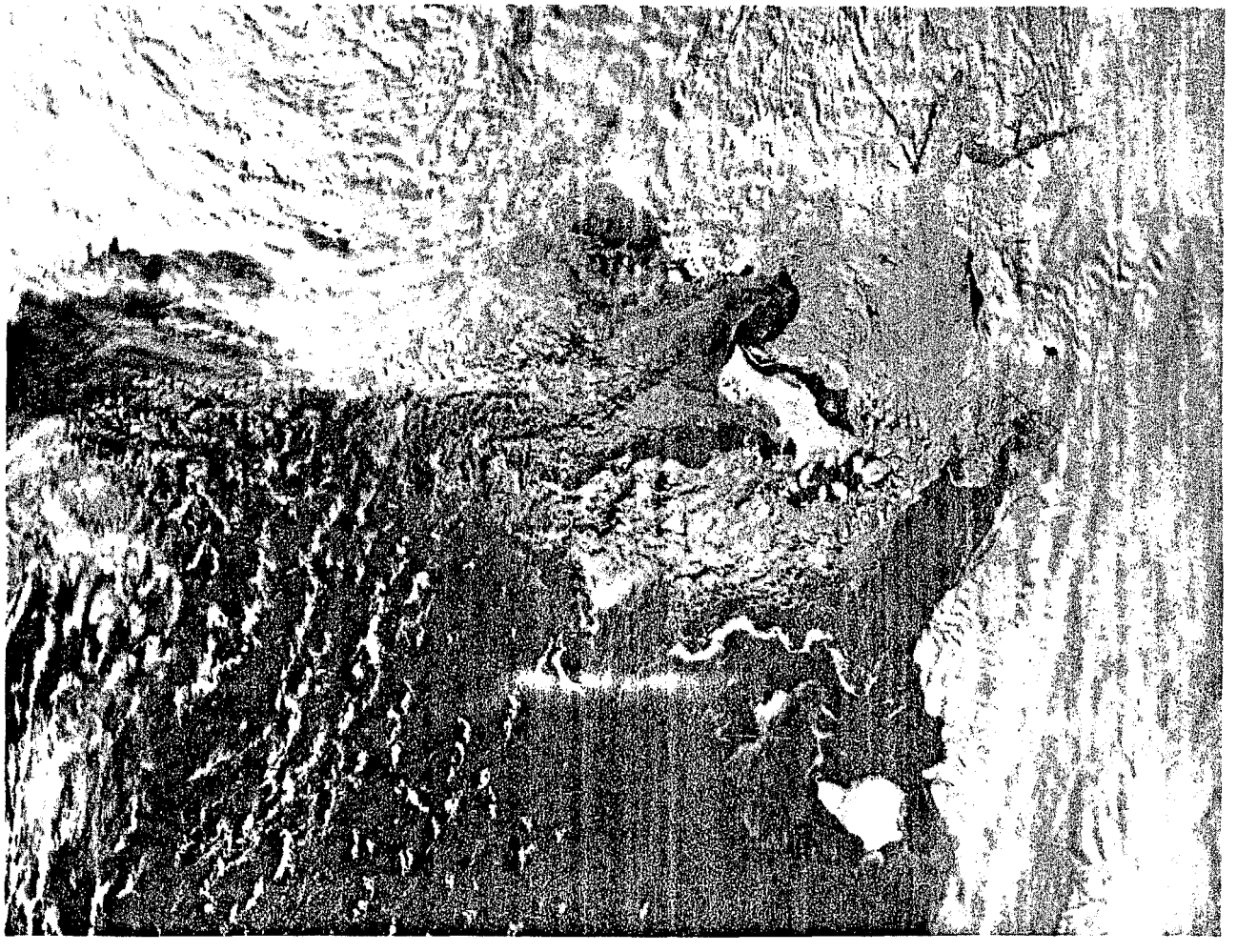

Figure 17a. Tiros image for 25 March (85:°124).

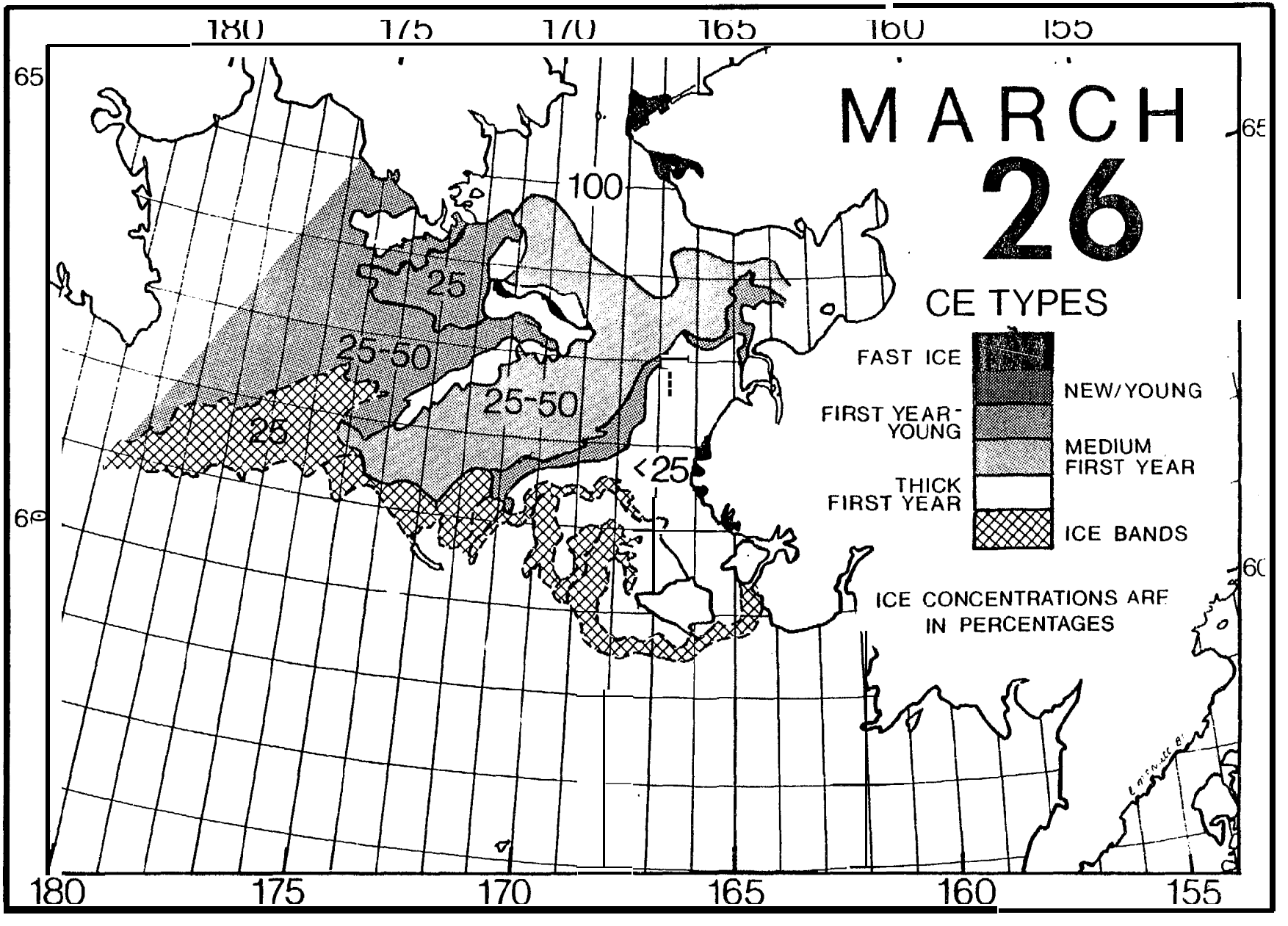

Figure 17b. Ice chart derived from Figure 17a.

Figure 18 shows the SMMR ice chart. As Table 1 shows, the SMMR image precedes the Tires image by only 3.5 hr, so that the two are nearly simultaneous . The letters on the SMMR image again mark areas of correspondence between the two images. First, the main ice edge "A", as shown by the location of the high gradient region, now extends north into Norton Sound. Second, "B*' marks the open water region adjacent to the coast shown in Figure 17a where, because of land contamination, the contours adjacent to the coast show an unobserved ice concentration increase. Third, continuing with the open water regions, "C'* marks the open water area north of Nunivak Island, and the elliptical 45% minimum contour marked by "D" is centered on the long narrow open water feature southwest of St. Lawrence Island. The long axis of the ellipse is nearly parallel to the axis of the open water feature, where the small lateral scale of the physical feature increases t-he apparent SMMR concentration. Similarly, "E" marks a more rectangular polynya north of the west end of St. Lawrence Island; and the concentration decrease marked by '*F" shows the cloud-obscured coastal polynya in the Gulf of Anadyr.

Fifth, "G" marks the 95% concentration region immediately south of the Bering Strait, where the southerly winds have created a high concentration ice jam. Also in this region, the 85% contour approximately follows the boundary between the thick and medium first-year ice shown in Figure 18. Finally, the 45-55% contour lines to the northwest of Nunivak Island correspond to the diffuse ice features in this region.

5. CONCLUDING REMARKS

The preceding discussion shows that, for the case of the Bering Sea in March, the high resolution SMMR channel produces uniformly good data

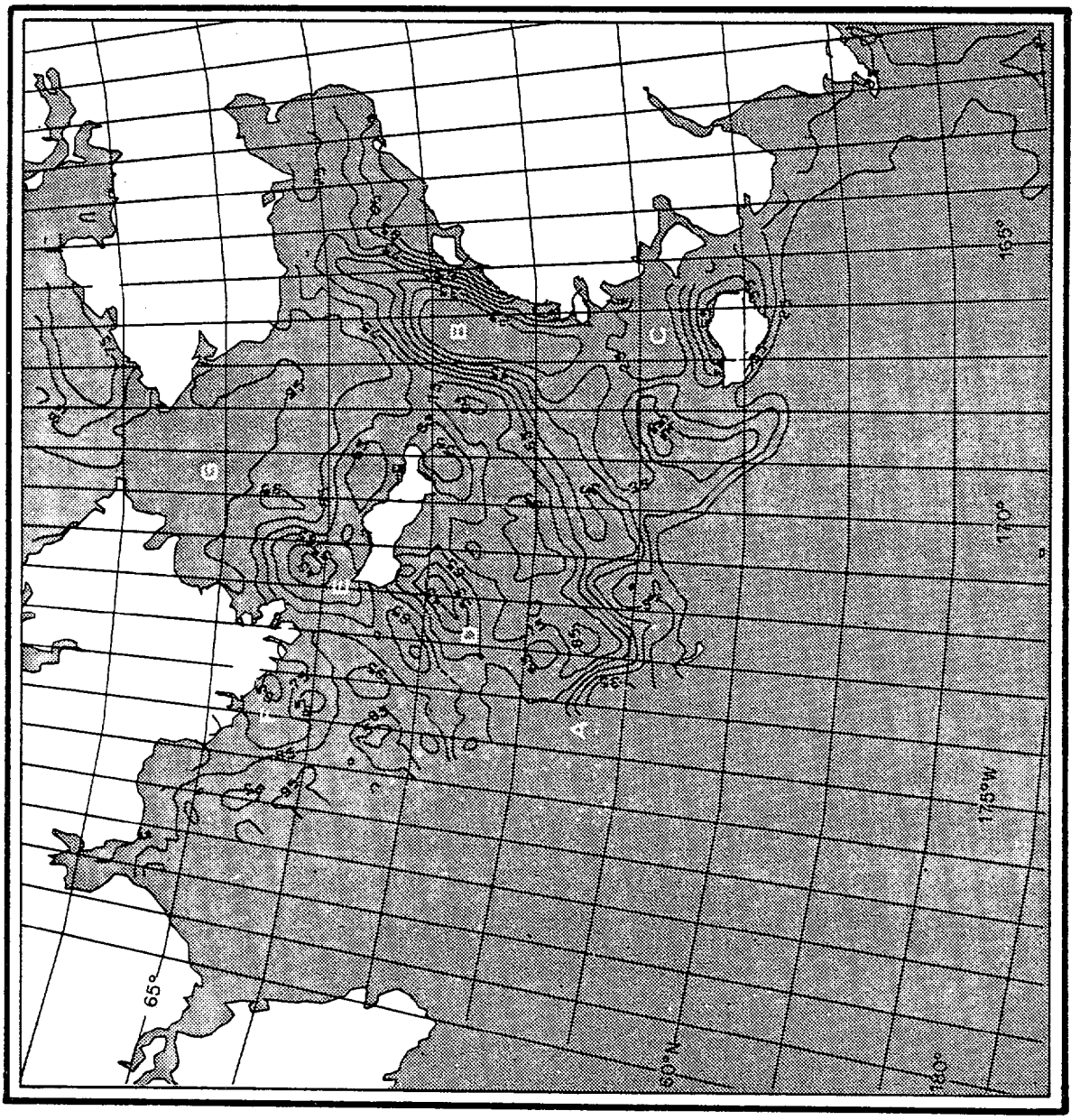

Figure 18. SMMR ice chart for day 84:2149. See text for further description.

regardless of weather. For each case, the SMMR mapped out the ice edge and the low and high concentration interior regions with an accuracy equal to that" of the derived ice charts. The only major difficulty in this algorithm comes from our lack of knowledge about thin ice emissivities, a lack which may produce some of the unrealistically low concentration values observed for thin ice. The other difficulty is that of land contamination, which can be anticipated. Finally, we hope that this work stimulates future work on both the measurement of thin ice emissivities and the application of this algorithm to other regions of first year sea ice such as the Labrador Sea and the Antarctic Ocean.

6. ACKNOWLEDGMENTS

This report received help and support from numerous sources. In particular, we thank Mr. William Abbott of NASA-Goddard for his help with the numerical work, Mr. K. F. Huemmrich of the Computer Sciences Corporation for implementing the SMMR ice algorithm, and Mr. Hugh Powell of Sigma Data Corporation for overcoming many of the technical difficulties in generating the final SMMR ice contour plots. We are also very grateful to the P-3 ice observer Lieutenant (jg) Daniel E. Munger and the pilot and crew of the Navy P-3, and to Captain James G. Grunwell and the officers and crew of the NOAA ship SURVEYOR. We also thank Ms. Carol Pease, who organized the weather data compilation cited in the text, arranged for the ice observer overflights, and provided help and encouragement in our analysis of the Bering Sea field data, and Dr. William Campbell, who provided valuable help with the early stages of this work. We further thank Ms. Frances Parmenter-Holt of the National Environmental Satellite Services field office in Anchorage for providing the satellite imagery, and Mr. Bruce Webster, who is the Alaska Regional

Ice Forecaster at the National Weather Service in Anchorage for providing ice advisories during the cruise.

During the period of this research, S. Martin gratefully acknowledges the support of the Department of Commerce Spacecraft Oceanography (SPOC) Group under contract MO-A01-00-4335, and thanks Dr. John Sherman and Mr. Henry Yotko for their encouragement and support. For the field portion of this work, he also acknowledges the support of the BLM/NOAA Outer Continental Shelf Program through Contract NA81RAC000-13. S. L. McNutt also acknowledges both the support of the SPOC group through Contract MO-A01-78-00-4335, and the support of NASA Contract NAG5-161. Finally, D. Cavalieri acknowledges support received from the NASA Oceanic Processes Branch under RTOP 146-40-08.

7. BIBLIOGRAPHY

Bauer, B.J. and S. Martin. 1980. Field observations of the Bering Sea ice edge properties during March 1979. Mon. Wea. Rev. 108:~045-56.

Gloersen, P. and F. Barath. 1977. A scanning multichannel microwave radiometer for Nimbus G and Seasat. IEEE J. Oceanic Engr. OE-2:172-78.

Gloersen, P., Wilheit, T.T., Chang, T.C., and W. Nordberg. 1974. Microwave maps of the polar ice of the earth. Bull. Am. Meteorol. Soc. 55:1442-48.

Gloersen, P., Zwally, H.J., Chang, A.T.C., Hall, D.K., Campbell, W.J. and R.O. Ramseier. 1978. Time-dependence of sea ice concentration and multiyear ice fraction in the Arctic Basin. Bdry. Layer Met. 13:339-59.

Martin, S. and P. Kauffman. 1979. Data Report on the Ice Cores taken during the March 1979 Bering Sea ice edge field cruise on the NOAA ship SURVEYOR. Special Report Number 89, Department of Oceanography (Department of Oceanography WB-10, University of Washington, Seattle WA 98195).

McNutt, S.L. 1981. Remote sensing analysis of ice growth and distribution in the Eastern Bering Sea. In: The Eastern Bering Sea Shelf: Oceanography and Resources, Volume One (Ed: Hood, D.W. and Calder, J.A.), National Oceanic and Atmospheric Administration, United States Department of Commerce, 141-66.

Pease, C.H. 1980. Eastern Bering Sea processes. Mon. Wea. Rev. 108:2015-23.

Sale, S.A., Pease, C.H. and R.W. Lindsay. 1980. Physical Environment of the Eastern Bering Sea, NOAA Technical Memorandum ERL PMEL-21, Pacific Marine Environmental Laboratory, Seattle WA, 119 pp.

Squire, V.A. and S.C. Moore. 1980. Direct measurement of the attenuation of ocean waves by pack ice. Nature, 283, No. 5745, 365-68.

Zwally, H.J., and P. Gloersen. 19771 Passive microwave images of the polar regions and research applications. Polar Record 18:431-50.

Appendix A. Verbatim Report of the P-3 Ice Reconnaissance Flight on 2 March 1979 (day 62)

AERIAL ICE RECON BERING SEA

1. RADAR ICE EDGE FM 6120N/17540W, TO 6124/17536, TO 6100/17440, TO 6102/17435, TO 6059/17415, TO 6033/17406, TO 6032/17330, TO 6024/17328, TO 6030/17320, TO COAST 6030N/17255W.

CONTINUING EDGE AT 6020N/17215W, TO 6024/17155, TO 6015/17135, TO 6012/17148, TO 5955/17135, TO 5958/17120, TO 6110/17112, TO 5950/17102, TO 5950/17050, TO 5955/17045, TO 5940/17050, TO 5938/17101, TO 5936/17115, TO 5934/17045, TO 5932/17102, TO 5931/17035, TO 5924/17040, TO 5921/17035, TO 5922/17025, TO 5920/17025, TO 5915/17015, TO 5858/17008, TO 5858/16958, TO 5840/16935, TO 5842/16930, TO 5830/16815, TO 5828/16812, TO 5826/16755, TO 5822/16735, TO END OF TRACK AT 5814N/15950W. -

2. TRACK FEATURES - SOUTHEAST TO NORTHWEST PORTION OF FLIGHT TRACK STRESSED VISUAL OBSERVATION OF PACK ICE GENERALLY 10-1 NM WITHIN THE ICE EDGE . NORTHWEST TO SOUTHEAST LEG WAS FOR DETAILED POSITIONING OF THE ICE EDGE BY VISUAL/RADAR OBSERVATION. THE FOLLOWING REPRESENTS A SYNOPOSIS OF SIG FEATURES ALONG, AND 10-1 5NM WITHIN THE BERING SEA ICE EDGE BETWEEN 16615W AND 17550W:

A) PREDOMINANT CONCENTRATION OF SURFACE COVERAGE OBSERVED -05-06 OKTAS

B) PREDOMINANT STAGES OF DEVELOPMENT - (BY PERCENT)

55 - GREY/GREY WHITE

40 - NEW/ YNG

05 - FIRST YEAR THIN (IN EXCESS OF 12 INCHES IN Thickness)

C) PREDOMINANT FORM OF ICE TOPOGRAPHY - (BY PERCENT)

70 - RAFTING

30 - NEW RIDGES

MAXIMUM OBSERVED RIDGES - 1 METER

D) PREDOMINANT FORMS OF ICE - (BY PERCENT)

40 - NEW ICE

30 - SMALL/MEDIUM FLOE

25 - BRASH/CAKE

05 - BIG, VAST, GIANT FLOE

3. SIGNIFICANT AREAS OF INTEREST -PARA 2 REPRESENTS THE GENERAL DESCRIPTION OF ICE ALG TRACK/WITHIN EDGE. FOLLOWING GIVES SPECIAL INTEREST AREAS DURING FLT:

A) HEAVIEST/THICKEST ICE WITHIN 10NM RADIUS OF 5952 F/170W. FIRST YR THIN WITH 30 PERCENT 1M NEW RIDGES

B) AREA OF LARGEST OBSERVED FLOES -WITHIN EDGE BETWEEN 16850W AND 16950W -25 PERCENT BIG/VAST FLOES.

C) AREA OF GREATEST CONCENTRATION - WITHIN EDGE BETWEEN 17245W AND 17530W - GENERALLY 07-08 OKTAS.

D) YOUNGEST/THINNEST ICE -01-05 NM ADJACENT EDGE ALG ENTIRE TRACK MOSTLY NEW ICE, NILAS, PANCAKE.

4. LOCALLY HIGH SURFACE WINDS ALG TRACK CAUSED CONSIDERABLE STRINGS OF ICE 02-05NM ADJACENT HVY PACK AT' SLIGHT RIGHT ANGLE TO WIND.

5. FLIGHT ADAK TO ADAK 6 PT ZERO HRS. LTJG MUNGER/AGC DAMICO SEND. NEXT SKED FLIGHT 08 OR 09 MARCH 79.